International Journal of Hydrogen Energy 255 (2026) 156400

Contents lists available at ScienceDirect

International Journal of Hydrogen Energy

journal homepage: www.elsevier.com/locate/he

Direct hydrogen production by cellulose aqueous phase reforming over NiMgAl hydrotalcite-derived catalyst: the counterintuitive effect of the addition of H_2

Emanuele Bosetti [a,b,c], Giulia Balestra [a,b,c], Jacopo De Maron [a,b,c], Eleonora Tosi Brandi [a,b,c], Andrea Fasolini [a,b,c,*], Francesco Basile [a,b,c,**]

[a] Department of Industrial Chemistry "Toso Montanari", University of Bologna, via Gobetti 85, Bologna, 40129, Italy
[b] Center for Chemical Catalysis – C^3, University of Bologna, via Gobetti 85, Bologna, 40129, Italy
[c] Interdepartmental Centre for Industrial Research, Renewable Sources Environment, Sea, Energy (CIRI-FRAME), University of Bologna, via Zamboni 33, Bologna, 40126, Italy

A B S T R A C T

Aqueous-phase reforming (APR) of cellulose is a process for sustainable hydrogen production and was investigated in this study using hydrotalcite-derived NiMgAl catalysts under optimized reaction conditions. Waste cellulose from the paper industry was employed as feedstock, highlighting the relevance of this approach within a circular economy and waste-to-hydrogen framework. Among the investigated Ni^0/Mg(Al)O formulations, $Ni_{24}Mg_{56}Al_{20}$ exhibited the best performance, providing an optimal balance between nickel loading, metal dispersion, and textural properties. The results indicate that hydrogen productivity is primarily governed by the availability and dispersion of metallic Ni species. In addition, different to previous studies, reaction conditions were investigated and the analysis of both gaseous and liquid products enabled the proposal of a reaction mechanism involving dehydration and hydrogenation/dehydrogenation pathways, which allowed to conceive effective strategies to increase hydrogen production.

For instance, a notable and counterintuitive outcome of this work is the beneficial effect of a moderate initial H_2 atmosphere. Controlled H_2 addition significantly enhanced hydrogen yields, reaching up to 40%, by promoting hydrogenolysis and reforming reactions while limiting condensation pathways associated with humin formation. In contrast, excessive H_2 partial pressure shifted the reaction network toward hydrogenation reactions, decreasing net hydrogen production. These findings highlight the crucial role of the reaction atmosphere in determining APR pathways.

The synthetized catalyst was compared with a benchmark Pt/Al_2O_3 catalyst tested under identical conditions, achieving superior hydrogen productivity and favouring reaction routes involving formic and levulinic acid intermediates, further contributing to hydrogen generation. Overall, the results demonstrate that properly engineered LDH-derived NiMgAl catalysts, combined with controlled reaction atmospheres, offer a cost-effective and sustainable alternative to noble-metal systems for hydrogen production from biomass and industrial waste streams.

1. Introduction

Climate change mitigation is one of the major challenges of our time, and the transition toward renewable energy systems that reduce dependence on fossil fuels is widely recognized as a key pathway [1]. Within this framework, hydrogen is expected to play a pivotal role, provided that sustainable solutions are developed for its production, storage, and utilization [2–4]. A key aspect of hydrogen production lies in its potential for delocalization, adapting generation routes to local territorial resources and, whenever possible, employing waste in the process [3–5]. Biomass represents a widespread and renewable carbon resource for the production of hydrogen and value-added chemicals [5–8]. Conventional thermochemical routes such as pyrolysis and gasification can produce hydrogen, but typically require high temperatures and significant energy input [5,9].

In this context, Aqueous Phase Reforming (APR) is a thermochemical catalytic process carried out in the liquid aqueous phase, enabling the production of hydrogen from oxygenated hydrocarbons [10]. APR is a promising solution for hydrogen production at moderate conditions (200-260 °C, 30-50 bars) from aqueous solutions of biomass-derived compounds [11], such as sugars, sugar alcohols, ethylene glycol and glycerol [12–14].

An additional advantage of APR is that the process operates under autogenous pressure, allowing the direct use of liquid oxygenated

* Corresponding author. Department of Industrial Chemistry "Toso Montanari", University of Bologna, via Gobetti 85, 40129, Bologna, Italy
** Corresponding author. Department of Industrial Chemistry "Toso Montanari", University of Bologna, via Gobetti 85, 40129, Bologna, Italy
E-mail address: andrea.fasolini2@unibo.it (A. Fasolini).

https://doi.org/10.1016/j.ijhydene.2026.156400
Received 26 March 2026; Received in revised form 31 May 2026; Accepted 2 July 2026
Available online 7 July 2026

feedstock streams without prior vaporization. Under these conditions, the water–gas shift (WGS) reaction occurs in situ, converting intermediate CO into CO_2, leading to a gaseous mixture containing a negligible amount of CO and enhancing hydrogen production [15–17]. Thus, APR can be described as the combination of two main steps: reforming reactions to yield carbon monoxide (CO) and hydrogen (H_2) (Eq. (1)), followed by the exothermic water-gas shift (WGS) (Eq. (2)), which can be combined to obtain the conventional reaction stoichiometry for APR (Eq. (3)):

$$C_nH_{2y}O_n \rightleftharpoons nCO + yH_2 \quad \text{(Eq. 1)}$$

$$CO + H_2O \rightleftharpoons CO_2 + H_2 \quad \text{(Eq. 2)}$$

$$C_nH_{2y}O_n + nH_2O \rightleftharpoons nCO_2 + (n+y)H_2 \quad \text{(Eq. 3)}$$

Typically APR is carried out over supported metal catalysts, e.g., Pt [18,19] and Ni [20] based catalysts. Critical issues for supports and active metals (e.g., textural properties and phase changes, leaching, and sintering) [21] were often reported for APR catalysts. Recent developments have shown that Pt/C or Pt/Al_2O_3 are promising candidates for the APR of a variety of organic components [22–28].

In a suitable catalyst for APR the metal phase must promote C–C, C–H and O–H bond cleavage while limiting C–O hydrogenolysis that would lead to hydrocarbon formation and reduced hydrogen yields [8,15]. In addition, catalysts should be active for the WGS reaction to convert CO and H_2O into H_2 and CO_2. While these transformations are mainly metal-catalysed, the support strongly influences APR performance depending on its physicochemical functionality. Acid–base sites on the support can facilitate O–H bond deprotonation and assist C–H activation on the metal surface. Metal particle size has also been shown to determine hydrogen production efficiency. These effects have been extensively studied for APR of alcohols and polyols [12,18,28].

While APR of model compounds is well established, the direct APR of cellulose (the major component of the lignocellulosic biomass) remains considerably less explored, despite representing an attractive and more practical route for hydrogen production [15,29,30]. Cellulose $(C_6H_{10}O_5)_n$ is a high–molecular-weight polymer composed of β-1, 4-linked D-glucose units (n ≈ 2000–20,000). In the aqueous-phase reforming pathway of cellulose, the reaction sequence is initiated by hydrolysis of the polymeric structure into glucose, after which successive C–H, O–H, and C–C bond cleavages take place, accompanied by the water–gas shift reaction (WGS) [31].

Compared to glucose APR, direct APR of cellulose remains scarcely investigated due to its structural complexity and the multiplicity of reaction pathways involved [29]. Cellulose hydrolysis and retro-aldol condensations represent crucial initial steps and can be catalysed by acid–base supports, while the metal phase governs hydrogen production. Nevertheless, elucidation of the reaction network for these larger molecules remains challenging; only limited work have addressed the mechanistic aspects, while most studies focus primarily on gaseous products [30,31].

Furthermore, cellulose is a solid feedstock, and its morphology and crystallinity influence dissolution and conversion. Microcrystalline cellulose is generally more susceptible to hydrolysis. Pre-treatments that reduce crystallinity (ball milling, steam explosion, sonication) can enhance hydrolysis but add complexity and cost to the process [32,33]. For this reason, many studies employ microcrystalline cellulose which, although useful for evaluating catalyst performance, only partially represents the complexity of real feedstocks [30,31,34–36].

In cellulose APR, the investigation of different catalysts based on both noble (Pt, Pd, Ir, 5% wt) or transition metals (Ni, Co, 20% wt) showed different catalytic performances toward reforming activity following Pt > Pd > Ir ≈ Co > Ni and hydrogen selectivity Pt > Ni > Pd ≈ Co > Ir [30,37]. In general, Pt provided the best results showing the highest conversion of carbon to gas (around 70%) and H_2 selectivity (around 40%) thanks to the high Pt C–C bond cleavage ability. Nevertheless, Ni represents a cost-effective alternative and is particularly attractive considering Pt inclusion in the European Union Critical Raw Materials list [38]. Although Ni intrinsic activity is generally lower than that of Pt, its performance can be enhanced through proper interaction with acid–base supports. In this perspective, layered double hydroxides (LDHs) are attractive precursors for designing Ni-based catalysts with high metal–support interfacial interaction [34,39,40]. Layered double hydroxides are a class of hydroxides composed of positively charged metal hydroxide layers (M^{2+} octahedra with a partial M^{2+}/M^{3+} substitution and a cation interspersion) and interlayer anions (A^{n-}) for charge compensation [41]. Their structure allows tuning of the M^{2+}/M^{3+} ratio and incorporation of different cations such as Ni^{2+}, Mg^{2+} and Al^{3+}, as adopted in this work. Upon calcination, LDHs transform into mixed oxides with high surface area while preserving cation dispersion. Subsequent reduction generates metallic nanoparticles (from reducible species such as Ni^{2+}) that segregate from the oxide matrix while maintaining strong interaction with the support. Moreover, LDH precursors enable straightforward tuning of acid–base properties and Ni content through precursor composition control [42,43].

These advantages were highlighted by Zhang et al. [34,36]; however, their work was limited to microcrystalline cellulose and did not thoroughly address the liquid-phase products. As a consequence, a deeper understanding of the reaction network occurring on real feedstocks is still missing, and improving this knowledge would provide valuable insights for future catalyst design. In addition, they did not investigate the reaction engineering conditions such as the presence of a reductive atmosphere and the use of real feedstocks like pulp cellulose, which are innovations carried out by the present work.

In this work, NiMgAl LDH-derived catalysts with different Ni contents were synthesized by co-precipitation and evaluated in the APR of a real cellulose feedstock derived from paper industry residues. In these catalysts, Ni provides the redox-active phase responsible for hydrogen production, while the MgAl mixed oxide contributes acid–base functionalities. Moreover, the effects of reaction time, initial H_2 atmosphere, and liquid product distribution were systematically investigated, enabling, beyond what was previously reported, the formulation of a mechanistic hypothesis for the complex reaction network of cellulose APR.

2. Materials and Methods

2.1. Materials

All reagents were purchased commercially without further purification. Na_2CO_3 (98%, Alfa Aesar), NaOH pellets (98%, Alfa Aesar), $Ni(NO_3)_2$*$6H_2O$ (99.9%, Alfa Aesar), $Al(NO_3)_3$*$9H_2O$ (98%, Sigma-Aldrich), $Mg(NO_3)2$*$6H_2O$ (99%, Sigma-Aldrich), $Pt(NH_3)_4(NO_3)_2$ (99.99%, Alfa Aesar, Premion®), Al_2O_3 (BASF, AL 3992 E 1/16), Lactic acid (90%, Fluka), Levulinic acid (98%, Sigma-Aldrich), Glucose (Fluka), Acetic Acid (99.8%, Sigma Aldrich), Propionic Acid (99.5%, Fluka), cellulose pulp (for its characterization see the Supplementary Materials).

2.2. Synthesis of the catalysts

2.2.1. Synthesis of NiMgAl LDH-based catalysts

The synthesis of the hydrotalcite supports was carried out using the co-precipitation technique at constant pH. For each catalyst, two separate aqueous solutions were prepared. The first solution contained the nitrates of the metal cations (cationic solution, $Mg(NO_3)_2{\cdot}6H_2O$, $Ni(NO_3)_2{\cdot}6H_2O$ and $Al(NO_3)_3{\cdot}9H_2O$) at molar ratios ensuring a total concentration of 2.0 M (the specific cation ratio varied depending on the catalyst synthesized). The catalysts were denoted as Ni0, Ni15, Ni24, and Ni35, according to their nominal nickel molar content (0, 15, 24, and 35 mol%, respectively). The anionic solution was prepared with

Na_2CO_3 1.0 M. The sodium carbonate solution was prepared under controlled temperature and pH conditions (56 °C, pH 10.5). The cationic solution was added dropwise to the anionic solution under constant stirring, maintaining the pH by addition of NaOH 2.0 M. After complete addition, the suspension was aged at 56 °C for 1 h. The resulting hydrotalcite was recovered by vacuum filtration, washed to neutral pH, dried at 70 °C overnight, and calcined at 650 °C for 12 h, yielding a mixed oxide with the desired cation molar ratios. The calcined powders were pelletized and sieved to 60–80 mesh. Catalyst reduction was performed in a stainless-steel tubular reactor by flowing an H_2/N_2 (10/90 v/v) mixture at 750 °C for 3 h, yielding the reduced metallic phase (Ni). (Fig. 1). The catalysts were reduced at 750 °C, although TPR analysis (see later) suggests that part of the Ni is reduced at higher temperatures. This has been done to preserve the mixed oxide structure, which decomposes to spinel and oxide above 750 °C as reported previously [44]. Nonetheless, the Ni reduction degree obtained with a TPR at 750 °C (Fig. S9) was 92%.

2.2.2. *Synthesis of the Pt/Al_2O_3 impregnated catalysts*

Commercial Al_2O_3 was loaded with Pt to obtain a final Pt loading of 3 wt% by incipient wetness impregnation [45] using $Pt(NH_3)_4(NO_3)_2$ dissolved in distilled water. The powders were put in an oven at 120 °C, then calcined heated up at 350 °C with a ramp of 2 °C/min and kept for 3 h. Reduction to Pt(0) phase was obtained by heating under a 10 mol% H_2 in nitrogen flow (100 mL/min) at 350 °C for 3 h.

2.3. *Characterization of the catalyst*

X–ray diffraction (XRD) analysis was carried out using a Philips PW1050/81 diffractometer equipped with a graphite monochromator in the diffracted beam and controlled by a PW1710 unit (Cu Kα, $\lambda = 0.15418$ nm). A 2θ range from 10° to 80° was investigated at a scanning speed of 40°/h. Scherrer equation was used to calculate the average crystallite size, which was approximated to the average particle size for the purpose of this work, though considering it as an approximation and better analysing particle size with TEM.

A TEM/STEM FEI TECNAI F20 instrument was used to analyse the morphology and metallic nanoparticles size distribution of reduced catalyst. Scanning electron microscopy (SEM) and energy dispersive spectrometry (EDS) were carried out with a Zeiss EP EVO 50 microscope and an INCA X-Act detector with PentaFET Precision. Spectra were recorded for 60 s with an accelerating voltage of 20 kV. The specific surface area of the catalysts was determined with the BET method by N_2 absorption-desorption at liquid N_2 temperature using a Sorpty 1750 Fison instrument (single-point BET) and a Belsorp MINI X instrument (Microtrac BEL). Temperature programmed reduction, pulse chemisorption of CO, and CO_2- and NH_3- desoprtion were performed using a Micromeritics Autochem II 2920 instrument equipped with a TCD detector. In TPR experiments, the catalyst was firstly heated to 180 °C with flowing He (20 mL/min), kept for 10 min. After cooling at 50 °C the TPR was performed by sending 20 mL/min of 5% v/v H_2/Ar over the sample, while the temperature was increased up to 950 °C at 10 °C/min, then kept at 950 °C for 30 min. Pulsed chemisorption of CO was carried out prereducing the sample in the same way as TPR experiments, but limiting the reduction temperature to 750 °C for 3 h; then, the sample was cooled down to 40 °C in a flux of 30 mL/min of He and subjected to 15 pulses of 10%CO/He (loop volume = 1000 μL). The same Micromeritics Autochem II 2920 instrument was used to investigate the acid and base properties of the samples by NH_3 and CO_2 temperature-programmed desorption (TPD). A pre-treatment in He at 7750 °C for 45 min was carried out to clean the catalyst surface from adsorbed water and carbonates. After cooling, the NH_3 chemisorption was conducted at 100 °C for 20 min by flowing 10% (v/v) NH_3/He at 30 mL/min, while the CO_2 chemisorption was conducted at 40 °C for 60 min by flowing 30 mL/min of 10% (v/v) CO_2/He. After chemisorption, the samples were flown with 30 mL/min of He for 60 min to remove the weakly physisorbed probe molecules. Finally, the temperature was increased from 50 °C to 650 °C at the rate of 10 °C/min constant heating rate, while the desorbed NH_3 or CO_2 was continuously monitored by the TCD detector.

Inductively Coupled Plasma–Atomic Emission Spectroscopy (ICP-AES) analyses were carried out using an Agilent 4210 MP-AES instrument to evaluate possible Ni leaching after APR reactions. Calibration curves were obtained using Ni standard solutions at 10 and 20 ppm, prepared from a $Ni(NO_3)_2$ solution in 0.5 mol L^{-1} HNO_3.

X-ray photoelectron spectroscopy (XPS) was carried out with an Axis Supra+ (KRATOS) spectrometer equipped with a monochromatic X-ray Al Kα radiation as the excitation source (1486.6 eV, 300·700 μm analysis area, 15 mA, 15 kV). The analysis chamber pressure was maintained lower than $5 \bullet 10^{-9}$ mmHg, sample charging was prevented with a charge neutralizer, and analysis were carried out with a hemispherical electron analyzer operating at constant pass energy (160 eV for survey spectra, 20 eV for high-resolution spectra). The energy scale was calibrated using Cu 2p3/2, Ag 3d5/2, and Au 4f7/2 photoelectron lines at 932.6, 368.2, and 83.9 eV, respectively.

Thermogravimetric analyses (TGA) were performed on a TA Instruments SDT Q600, under air atmosphere (flow rate: 100 mL/min) up to 700 °C.

2.4. *APR reaction - experimental setup and procedure*

Catalytic tests were carried out in a 300 mL stainless-steel Parr autoclave, loaded with 0.45 g of catalyst, 1.50 g of substrate and 50 mL of ultrapure water. Prior to the reaction, the system was purged with N_2 to remove residual oxygen, then heated from atmospheric pressure to 250 °C (or 200 °C for the test with Ni0 used to spot reaction intermediates) and maintained at this temperature for 3 h under autogenous pressure, before rapid cooling with ice. Reaction times reported exclude the heating period. Some tests were conducted under the same conditions but using reaction intermediates (e.g. ethylene glycol, pyruvaldehyde, glycolaldehyde, formic acid) to get insight into the reaction pathways generating from them. After reaction, the gas phase was analysed off-line by GC equipped with molecular sieves and carbon plot columns and TCD detectors. Liquid products, obtained after catalyst removal by filtration, were analysed by HPLC using a Rezex ROA Organic Acid column with 0.0025 M H_2SO_4 as mobile phase

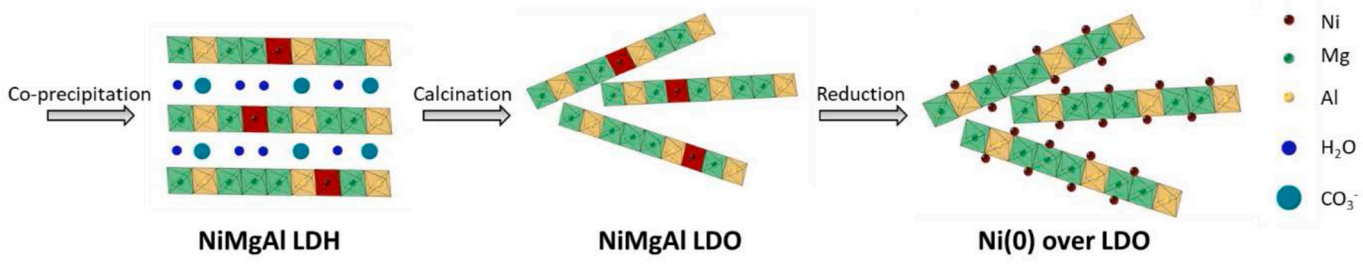

Fig. 1. Schematization of the NiMgAl hydrotalcite-derived catalyst preparation procedure.

(0.5 mL min^{-1}) and DAD/RID detection.

The reaction generates a complex mixture of liquid-phase products and polymeric species (humins) [46–50], as visual formation of insoluble black material occurs. As a result, most of the literature studies of cellulose and oxygenate products APR report only gaseous products or a limited set of liquid compounds [30,31,36,39,50]. In the present work, the identification and quantification of the main liquid products were carried out with the aim of elucidating the main reaction pathways. However, the HPLC analysis revealed the presence of several additional peaks that could not be confidently identified or quantified. However, the amount of carbon present in the liquid phase after reaction was determined with a total organic carbon analyzer (mod. TOC-L, Shimadzu). The TC content was determined after the thermal oxidation to CO_2 by using a detector working in the IR range. Agilent Technologies HPLC 1260 infinity II equipped with a Poroshell 120 mm 2.7 μm column and with Mass Spectrometer was used to identify the mass of the oligomers showing products with mass equal or higher than 573 *m/z*. Agilent Cary 630 ATR FT-IR spectrometer with transmission analysis module (FT-IR) and attenuated total reflection (ATR, diamond crystal) analysis module was used to analyse the obtained solid which was also accurately weighted.

2.4.1. Products yield and productivity calculations

The yields of gaseous products were calculated as the average of the last four GC injections. The amount of gaseous product B was determined according to Eq. (4), based on the ideal gas law:

$$Y_B(\%) = \frac{\left(\frac{Area_B}{F_B}\right)}{n_{tot\ syringe}} \times \frac{P_{system} \times V_{system}}{0{,}083145 \times T(K)} - n_{in\ B} \Big/ n_{cellulose} \times 6 \times 100 \quad \text{(Eq. 4)}$$

where:

- $Area_B$ is the GC peak area of product B
- F_B is the calibration factor of compound B
- $n_{tot\ syringe}$ is the total number of moles contained in the gas volume injected into the GC
- P_{system} is the reactor pressure at sampling conditions (bar)
- V_{system} is the gas-phase volume of the reactor (L)
- R is the ideal gas constant (0.083145 L bar $mol^{-1} \cdot K^{-1}$)
- T is the temperature at which the gas is considered (K)
- $n_{in}B$ is the initial amount (mol) of compound B present in the reactor before reaction
- $n_{cellulose}$ is the number of moles of cellulose, calculated using the monomer molecular weight (162.14 g mol^{-1})

The factor 6 accounts for the number of carbon atoms per glucose unit.

For all products except hydrogen, $n_{in}B = 0$. For H_2, $n_{in}B$ corresponds to the amount of hydrogen initially charged in the reactor in experiments carried out under an H_2 atmosphere; in all other cases, it is equal to zero.

The yields of liquid products were calculated as follows:

$$Y_B(\%) = \frac{\left(\frac{Area_B}{F_B}\right) \times \frac{V_{final}\ (L)}{1000}}{mol_{cellulose}} \times 100 \quad \text{(Eq. 5)}$$

where:

- $Area_B$ is the HPLC peak area of product B
- V_{final} is the final volume of the liquid phase (mL)

These formulas facilitate the quantification of both gas and liquid product yields in relation to the amount of cellulose used in the reactions.

The hydrogen productivity was determined by dividing the total amount of H_2 produced at the end of the reaction by the reaction time and the catalyst mass and was expressed as $mmol_{H2} \cdot h^{-1} \cdot g_{CAT}^{-1}$.

3. Results

3.1. Catalysts characterization

3.1.1. NiMgAl LD-based catalysts characterization

After the coprecipitation synthesis the formation of the hydrotalcite precursor of the catalysts was confirmed by XRD analysis. Fig. 2-A shows the XRD patterns of the hydrotalcite precursors after drying and calcination. All samples display the characteristic reflections of carbonate-intercalated hydrotalcite ($Mg_6Al_2CO_3(OH)_{16} \cdot 4H_2O$), in agreement with crystallographic databases. The three typical basal reflections observed at about 11.7, 23.6 and 35.4°, with interplanar spacing ratios of 6:3:2, can be indexed to the (003), (006), and (009) planes, corresponding respectively to one, two, and three layers of the layered double hydroxide structure, confirming the successful formation of the hydrotalcite phase containing Ni, Mg and Al in the cationic layer. Upon calcination at 650 °C for 12 h, the hydrotalcite structure decomposed due to the removal of hydroxyl groups and interlayer carbonates, resulting in the release of H_2O and CO_2 and the collapse of the layered structure. This transformation results in the formation of a homogeneous Ni–Mg–Al mixed oxide (LDO) with a MgO-like structure, as confirmed by the XRD patterns of the calcined samples (Fig. 2-B).

After reduction, the NiO species present in the mixed oxide structure are reduced and segregate from the lattice with an ex-solution process, forming metallic Ni nanoparticles dispersed on the Mg–Al mixed oxide support. As shown in Fig. 2-D, the XRD patterns of the reduced samples clearly display the characteristic reflections of metallic Ni at approximately 45, 53 and 76° (2θ). With increasing Ni content, the relative intensity of metallic Ni reflections progressively increases, becoming predominant for Ni35, consistent with the higher nickel loading in the catalyst. The average Ni crystallite size was estimated from the XRD patterns of the reduced catalysts using the Debye–Scherrer equation. Only the Ni reflection at ~53° (2θ) corresponding to the Ni(200) plane, was used for the calculation, as the peak at ~76° is too weak to provide reliable estimates, while the reflection at ~45° overlaps with the mixed oxide peak, hindering accurate analysis. The results are summarized in Table 1 and indicate that increasing the Ni loading leads to larger Ni crystallites, due to enhanced aggregation of Ni atoms during reduction; in particular, the Ni35 catalyst exhibits the largest crystallite size (≈23.9 nm), consistent with its higher nickel content. However, it should be noted that crystallite sizes estimated by the Scherrer equation provide only an average approximation based on XRD peak broadening and may overestimate particle dimensions due to the contribution of particle agglomeration and structural effects.

The textural properties of the catalysts were evaluated by N_2 physisorption measurements, and the specific surface areas are reported in Table 1. The Ni0 sample exhibits the highest surface area (171 $m^2\ g^{-1}$), reflecting the highly porous mixed oxide framework derived from the LDH precursor. Upon nickel incorporation and reduction, a progressive decrease in surface area is observed with increasing Ni loading. Among the Ni-containing samples, Ni15 shows the highest specific surface area (133 $m^2\ g^{-1}$), followed by Ni24 (90 $m^2\ g^{-1}$), whereas Ni35 displays a markedly reduced value (44 $m^2\ g^{-1}$). Nitrogen physisorption isotherms and pore distribution, is reported in Figs. S1–6 and Table S2 together with total pore volume and average pore diameter. The pore diameter enlarges for the Ni35 samples indicating a morphology modification.

This trend is fully consistent with the XRD results of the reduced materials. As demonstrated by Scherrer calculations, increasing Ni content leads to the formation of progressively larger metallic Ni crystallites, whose ex-solution from the mixed oxide may produce morphology changes with reduction of surface area In the case of Ni35, the high amount of ex-soluted Ni is associated with a pronounced loss of

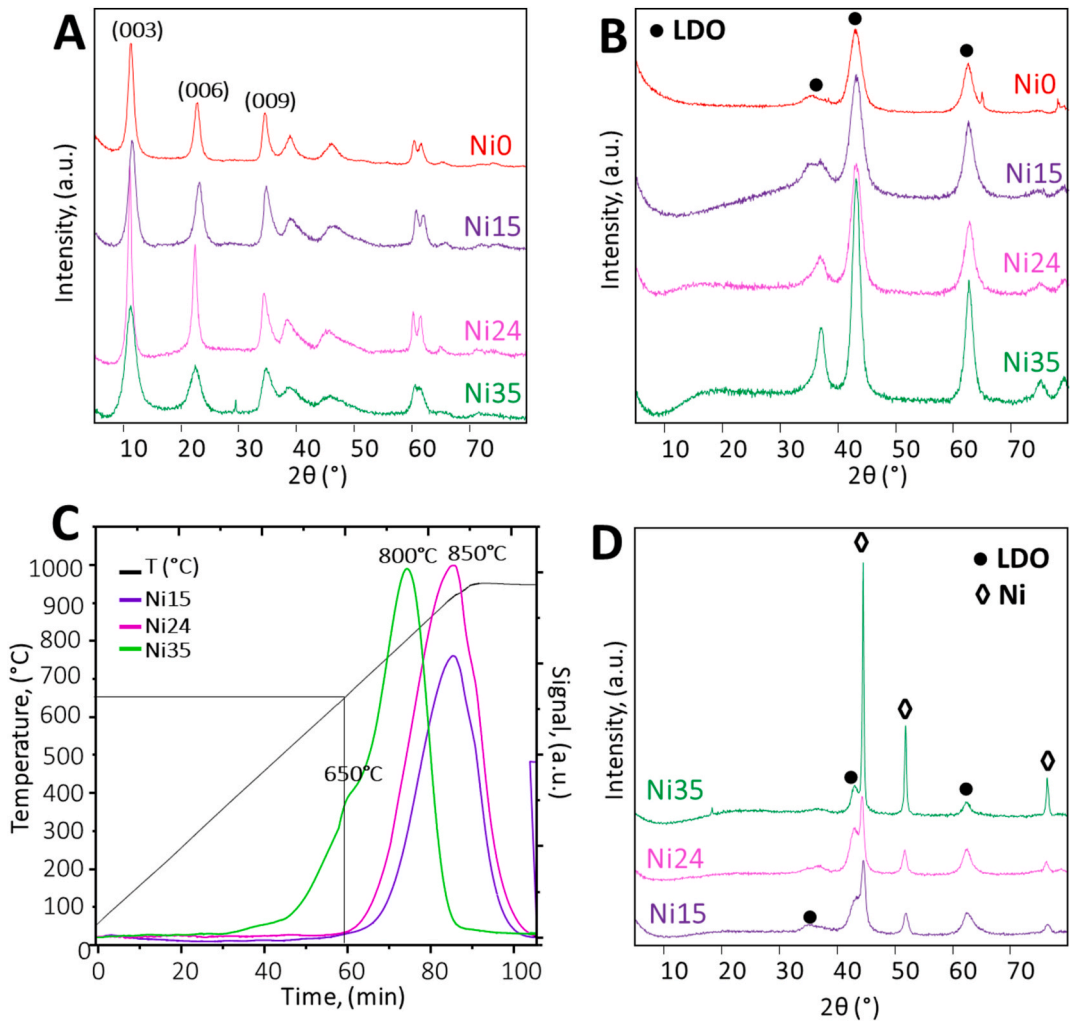

Fig. 2. XRD patterns of (A) dried samples, (B) calcined samples at 650 °C and (D) reduced samples at 750 °C. Temperature programmed reduction (TPR) for Ni-containing samples (C).

Table 1
Nominal molar composition and BET specific surface area of the reduced catalysts.

Catalyst	Molar content (%)[a]			BET SSA (m^2/g)[b]	d_{Ni} (nm)[c]	Reduction temperature (°C)[d]		Acid-base properties[e]			%Ni dispersion[f]
	Ni	Mg	Al			T_R start	T_R max	Acidity ($mmol_{NH3}$/g)	Basicity ($mmol_{CO2}$/g)	A/B	
Ni0	-	75	25	171	-	-	-	0.32	0.81	0.40	-
Ni15	15 (13)*	57 (60)*	28 (27)*	133	8,7	650	850	0.35	0.57	0.61	1.21
Ni24	24 (26)*	56 (54)*	20 (20)*	90	14,0	650	850	0.36	0.23	1.55	1.07
Ni35	35 (38)*	45 (44)*	20 (18)*	44	23,9	400	650-800	0.27	0.49	0.55	1.81

[a] Nominal molar composition based on synthesis stoichiometry.
[b] N_2 physisorption.
[c] Debye-Scherrer equation from XRD data of Ni(200) plane.
[d] TPR analysis.
[e] TPD-NH_3 and TPD-CO_2 analysis.
[f] TPD-CO analysis. *actual Ni, Mg and Al molar content obtained by SEM-EDS with a standard deviation of ±0.2.

textural properties. Conversely, the higher aluminium content in Ni15 contributes to improved structural stability of the mixed oxide matrix, limiting metal particle growth and preserving porosity. Ni24 represents a balanced formulation, combining a relatively high surface area with an adequate nickel content.

SEM analysis was used to probe the actual concentration of Ni, Mg and Al in the Ni15, Ni24 and Ni35 mixed oxides, which is reported in Table 1. The results show a similar composition to the nominal one.

Further characterization of the Ni-containing catalysts was carried out by H_2 temperature-programmed reduction (H_2-TPR) and the corresponding results are reported in Fig. 2-C and Table 1, where the peaks correspond to the reduction of Ni^{2+} to Ni^0. The H_2-TPR profiles of both

Ni15 and Ni24 display a broad reduction peak in the high-temperature region (650–950 °C), which can be ascribed to the reduction of strongly interacting Ni species embedded in the mixed oxide matrix, indicative of a strong metal–support interaction and of the ex-solution process. A higher-intensity reduction peak is observed for Ni24, in agreement with its higher Ni content. In contrast, the H_2-TPR profile of Ni35 exhibits an additional shoulder at lower temperatures (400–650 °C), which can be attributed to the reduction of NiO bulk species more available on the catalyst surface and therefore more readily reducible, thanks to the higher Ni amount [30]. The H_2-TPR profiles were integrated in order to estimate the reduction degree of the catalysts. The calculated reduction degrees were 80.9%, 86.1%, and 83.5% for Ni15, Ni24, and Ni35, respectively. The slightly higher reducibility observed for Ni24 suggests a favourable balance between Ni dispersion and metal–support interaction. Overall, the TPR analyses indicate that nickel reduction predominantly occurs above 650 °C for all catalysts. Accordingly, a reduction temperature of 750 °C was selected to ensure a complete and homogeneous reduction of the nickel species before catalytic testing.

To further characterize the surface chemistry of the real active phase, Ni24 was selected for *ex situ* XPS analysis after the same prereduction procedure used before catalytic testing (i.e., 750 °C for 3 h). All the photoelectron and Auger lines in the survey spectrum of Ni24 (Fig. S14a) could be attributed to either magnesium (Mg KLL, Mg 2s, Mg 2p), nickel (Ni 2p, Ni LMMa-d, Ni 3s, Ni 3p), aluminium (Al 2s, Al KLL, Al 2p), oxygen (O1s, O2s, and O KLL), and adventitious carbon (C1s). The high-resolution spectra for the Ni 2p and O1s core levels of pre-reduced Ni24 are shown in Fig. 3a and b. The Ni 2p core level region is characterized by the presence of both metallic nickel ($2p_{3/2}$ BE = 851.6 eV, spin orbit splitting = 17.8 eV) and Ni^{2+} species ($2p_{3/2}$ BE = 854.2 eV, spin orbit splitting = 18.5 eV [51], coexisting on the pre-reduced ex-LDH catalyst surface. The formation of Ni^{2+} species can be assigned to the interaction of metallic Ni produced during reduction and the oxygen of the support, favoured by the ex-solution process and suggesting a good metal support interaction. The latter can positively influence hydrogen production and push the reaction mechanism toward the cleavage of C–C and C–H bond as previously reported [34]. The O 1s region displayed an asymmetric peak that was deconvoluted into 2 contributions centred at 530.0 eV and 531.8 eV, which have been attributed to lattice oxygen and low-coordination oxygen (O_{LC}) respectively. Overall, these results are in good agreement with the available literature on pre-reduced Ni-based ex-LDH catalysts [34,52]. The Al 2p region was characterized by a partial overlap of the Al 2p photoelectron line (BE = 73.9 eV, Al^{3+}) with the one of Ni 3p, while the Mg 1s region was characterized by a peak centred at 1304 eV (Mg^{2+} in MgO-like oxides); finally, the high-resolution spectrum of the C1s core level was characterized by 2 contributions centred at BE = 284.6 eV (C–C and C–H species in adventitious carbon) and BE = 289.3 eV (carbonates species) [53] these spectra are reported in Fig. S14b–d.

In addition, CO chemisorption measurements were carried out to estimate the amount of exposed metallic Ni sites and the corresponding Ni dispersion. The obtained CO uptakes were 33.9, 42.1, and 104.7 $\mu mol_{CO} \cdot g_{CAT}^{-1}$ for Ni15, Ni24, and Ni35, respectively, corresponding to apparent Ni dispersions of 1.21%, 1.07%, and 1.81% (Table 1). The significantly higher CO uptake observed for Ni35 suggests a larger amount of exposed Ni species, likely associated with the higher Ni loading and the presence of more surface-accessible bulk-like Ni domains.

The dispersion of the metallic phase in the selected Ni24 catalyst was further investigated by TEM analysis for all reduced Ni-containing catalysts (Fig. 4), confirming the formation of well-dispersed metallic Ni nanoparticles. The particle size distribution was obtained by measuring 300 nanoparticles for each sample. All catalysts displayed particle size distributions mainly comprised between 10 and 20 nm, with only a limited fraction of larger particles, indicating effective dispersion of the active phase upon reduction promoted by the ex-solution process and the strong metal–support interaction. The particle sizes estimated from TEM analyses differ from those obtained by XRD-Scherrer calculations. While the Scherrer equation provides an average estimation based on crystallite diffraction broadening, TEM measurements are considered more reliable for direct particle size determination.

Further characterization of the surface acid–base properties of the reduced catalysts was carried out by NH_3-TPD and CO_2-TPD analyses after reduction at 750 °C, i.e., under the same conditions adopted before catalytic testing. The corresponding desorption profiles are reported in Fig. 5, while the total acidity, total basicity, and acid/base ratio (A/B) are summarized in Table 1. The same analyses were also performed on the Ni0 catalyst to evaluate the effect of Ni introduction on the acid–base properties of the mixed oxide system.

The CO_2-TPD profiles exhibit partially overlapping desorption peaks, indicating the coexistence of basic sites with different strengths. As widely reported in the literature, hydrotalcite-derived catalysts typically display three distinct CO_2 desorption regions [54].

According to the desorption temperature, these regions can be attributed to weak basic sites (100–140 °C), medium-strength basic sites (240–280 °C), and strong basic sites (around 400 °C). The low-temperature peak is associated with weak Brønsted basic sites, arising from the decomposition of bicarbonate species formed by the interaction of CO_2 with surface hydroxyl groups. The medium-temperature peak corresponds to Lewis basic sites related to bidentate carbonate species coordinated to metal–oxygen pairs. Finally, the high-temperature desorption peak is assigned to CO_2 chemisorbed on low-coordination

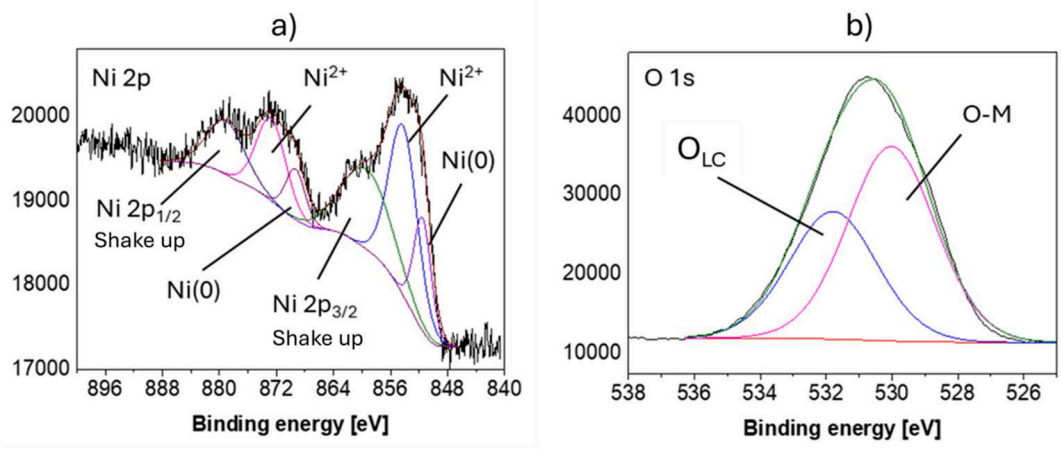

Fig. 3. High resolution ex situ XPS spectra of Ni24 after prereduction for 3 h at 750 °C: a) Ni 2p and b) O 1s.

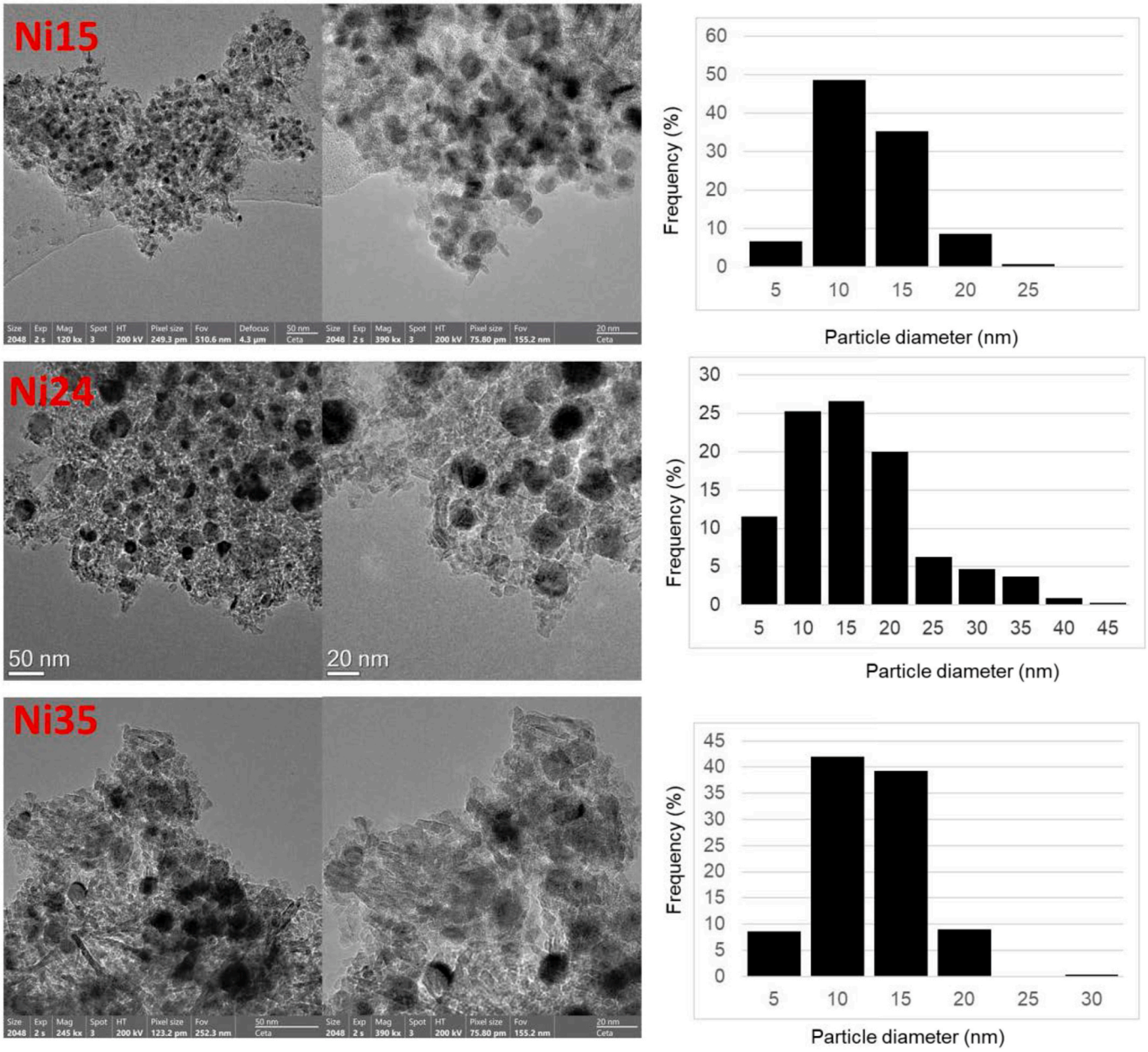

Fig. 4. TEM and STEM analyses images and particle size distribution of Ni nanoparticles in the reduced Ni15, Ni24 and Ni35 catalysts The distribution was obtained by measuring 300 nanoparticles.

oxygen anions, corresponding to strong Lewis basic sites.

The Ni0 catalyst exhibited the highest total basicity among the investigated samples (0.81 $mmol_{CO2}\cdot g^{-1}$) together with the lowest A/B ratio (0.40), indicating a predominantly basic character before Ni incorporation. In the CO_2-TPD profile of Ni0, a single broad desorption contribution centred around 200 °C is observed, indicating mainly medium-strength basic sites. Upon Ni incorporation, new desorption contributions appear at higher temperatures, indicating the formation of stronger basic sites associated with modifications in the mixed oxide structure induced by Ni addition.

The total basicity does not follow a linear trend with the Ni content. Ni15 exhibited the highest amount of basic sites, with a total basicity of 0.57 $mmol_{CO2}\ g^{-1}$, followed by Ni35 (0.49 $mmol_{CO2}\ g^{-1}$), whereas Ni24 showed the lowest value (0.23 $mmol_{CO2}\ g^{-1}$). This behaviour suggests that the amount and accessibility of basic sites are influenced not only by the nominal Ni loading, but also by the distribution of Ni, Mg, and Al species in the mixed oxide matrix. In particular, Ni15 displays a broad desorption contribution centred around 230 °C, attributable to medium-strength basic sites, together with a second contribution around 450 °C associated with strong basic sites. The broadness of the profile suggests the partial overlap of different populations of medium-strength basic sites. Ni24 exhibits a less intense and narrower desorption profile, indicating a lower concentration of accessible basic sites. In contrast, Ni35 shows desorption features distributed over a broader temperature range, indicating the coexistence of weak, medium, and strong basic sites.

The NH_3-TPD profiles reflect the thermal desorption of ammonia molecules previously adsorbed on acid sites of different strength. The Ni0 catalyst exhibits a single desorption contribution centred around 180 °C, corresponding mainly to weak acid sites. Upon Ni incorporation, additional desorption contributions at higher temperatures appear, indicating the formation of stronger acid sites. The profiles of the three catalysts are overall more similar than those observed in CO_2-TPD, especially in the case of Ni15 and Ni24. Both samples display a first

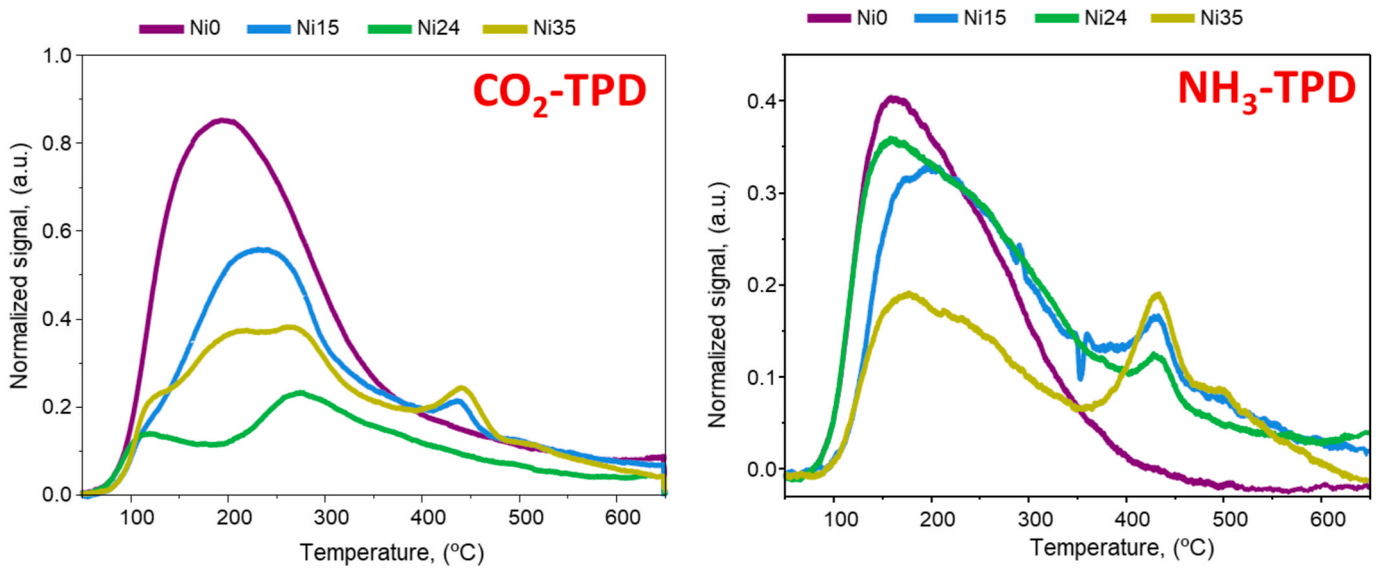

Fig. 5. CO_2-TPD (left) and NH_3-TPD (right) profiles of Ni0, Ni15, N24 and Ni35 catalysts.

broad desorption band extending from 120 to 350 °C, characterized by a shoulder, indicating the coexistence of weak and medium-strength acid sites and suggesting the contribution of more than one overlapping component. In addition, a distinct peak observed at approximately 450 °C can be attributed to strong acid sites, where ammonia is more strongly coordinated. Compared with Ni15, Ni24 appears to exhibit a slightly higher contribution of medium-strength acid sites together with a slight decrease in strong acid sites. Ni35 presents the same main desorption regions, but with different relative intensities: the contributions associated with weak and medium-strength acid sites are reduced, whereas the high-temperature contribution related to stronger acid sites becomes more pronounced. The total acidity values of Ni15 and Ni24 are very similar, amounting to 0.35 and 0.36 $mmol_{NH3}\ g^{-1}$, respectively, while Ni35 exhibits a lower total acidity of 0.27 $mmol_{NH3}\ g^{-1}$. These results indicate that increasing the Ni content generally leads to a decrease in the total acidity of the reduced catalysts, although the distribution of acid site strength does not follow a strictly linear trend.

Overall, the coexistence of measurable amounts of both acidic and basic sites demonstrates the amphoteric nature of the reduced NiMgAl catalysts. Ni24 exhibited the highest acid/base ratio (A/B = 1.55), significantly higher than Ni(0.40), Ni15 (0.61) and Ni35 (0.55), indicating a predominance of acidic functionalities at the catalyst surface. This result is consistent with the findings reported by Casenave et al.

[55] who observed that the substitution of Mg by Ni in LDH-derived NiMgAl catalysts leads to an increase in surface acidity. In addition, Gac [56] demonstrated that after reduction the relative acidity of these systems is enhanced. Therefore, an enhanced acidic character was expected for the present Ni-containing materials. The more balanced amphoteric character of Ni24, combined with an adequate amount and dispersion of metallic Ni, may favour the coexistence of hydrolysis, retro-aldol, hydrogenolysis, and reforming pathways during cellulose APR, contributing to the superior catalytic performance observed for this catalyst.

3.1.2. *Pt/Al_2O_3 impregnated catalyst characterization*

The Pt/Al_2O_3 catalyst was characterized to enable a more rigorous comparison with the NiMgAl-derived systems. SEM-EDS analysis revealed a Pt content of approximately 2.7 ± 0.2 wt%, in good agreement with the nominal loading of 3 wt%, confirming the effectiveness of the impregnation procedure. BET analysis showed a specific surface area of 98 $m^2\ g^{-1}$ after reduction.

CO chemisorption measurements were additionally carried out to estimate the amount of exposed Pt sites. The Pt/Al_2O_3 catalyst exhibited a CO uptake of 31.11 $\mu mol_{CO} \cdot g_{CAT}^{-1}$, which was subsequently used for turnover frequency (TOF) calculations assuming a CO/metal surface stoichiometry of 1:1.

3.2. *Catalytic activity of NiMgAl catalysts in the APR reaction*

3.2.1. *Role of nickel on cellulose APR*

To evaluate the role of nickel content and presence on APR of cellulose pulp performance, catalytic tests were carried out under identical conditions (250 °C, 3 h, 1.50 g of cellulose pulp, 0.45 g of catalyst and under 1 atm of N_2 atmosphere) using the reduced catalysts Ni15, Ni24, and Ni35, with nominal nickel content of 15, 24 and 35 mol%, respectively, as well as a blank test (without catalyst) and a Ni-free MgAl hydrotalcite-derived mixed oxide (Ni0). The yields of gaseous and liquid products, together with the hydrogen productivity expressed as $mmol_{H2} \cdot h^{-1}\ g_{CAT}^{-1}$, calculated as the total amount of H_2 produced at the end of the reaction divided by the reaction time and the catalyst mass, are summarized in Figs. 6 and 7.

As depicted in Fig. 6, hydrogen production is negligible in both the

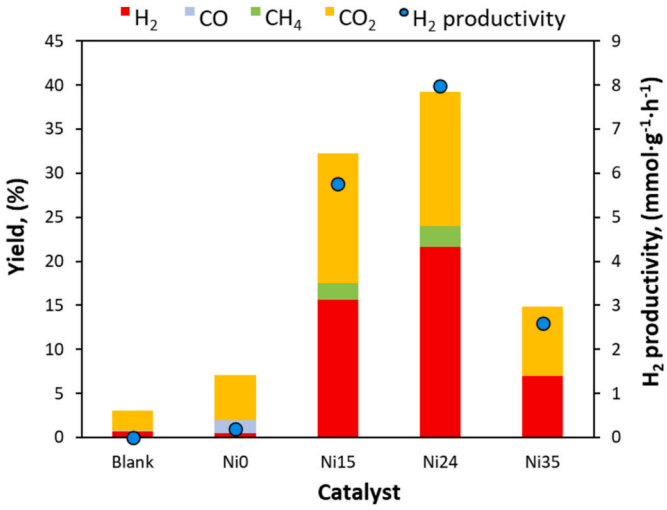

Fig. 6. Effect of the Ni presence and nominal Ni molar content (mol %) over the gaseous products yields and H_2 productivity during APR of cellulose. 250 °C, 1.5 g cellulose. 0.45 g cat., 50 mL water, 3 h, N_2 atm.

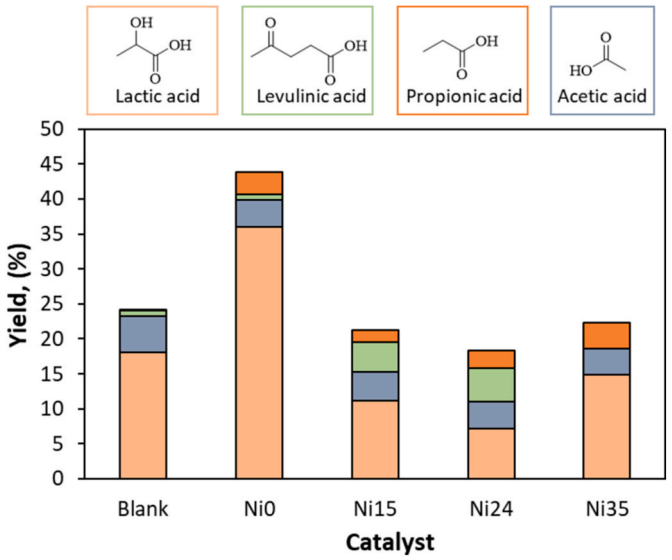

Fig. 7. Effect of the Ni presence and nominal Ni molar content (mol %) over the liquid products yields during APR of cellulose. 250 °C, 1.5 g cellulose. 0.45 g cat., 50 mL water, 3 h, N_2 atm.

blank test and over the Ni0 catalyst, indicating that hydrogen formation occurs almost exclusively in the presence of metallic Ni. This suggests that, while the acid-base properties of ex-hydrotalcite MgAl mixed oxides may promote cellulose hydrolysis to glucose as well as isomerization and retro-aldol condensation reactions [55,57,58], the subsequent dehydrogenation, hydrogenolysis, hydrogenation, and reforming steps required for hydrogen production are governed by metallic Ni sites.

Among the Ni-containing catalysts, Ni15 shows limited hydrogen production despite its relatively high surface area. Hydrogen yield and productivity are instead mainly controlled by the amount and dispersion of metallic Ni. Increasing the Ni loading to 24 mol% markedly enhances catalytic performance, leading to the highest hydrogen productivity (8 $mmol_{H2}.g_{CAT}^{-1}.h^{-1}$). Conversely, a further increase to 35 mol% causes a sharp decline in hydrogen production due to Ni particle sintering during reduction, as evidenced by XRD, and a severe loss of surface area (44 $m^2\ g^{-1}$).

CO_2 formation originates from C–C cleavage of C_2 intermediates and from water–gas shift reactions, whereas CH_4 can be produced via C–C cleavage followed by hydrogen recombination, reforming of oxygenated intermediates (e.g., methanol and ethanol), or CO/CO_2 methanation [45]. Methanol and ethanol, formed through hydrogenation of ethylene glycol, further contribute to hydrogen production via reforming reactions, where firstly the cleavage of the C–H and/or O–H bonds by dehydrogenation leads to the formation of CO intermediate. The CO is then converted to CO_2 and H_2 through the water–gas shift reaction (WGS), assisted by the dissociated hydroxyl groups adsorbed from water [29].

Ethylene glycol, which derives from the hydrogenation of glycolaldehyde, formed from retro-aldol condensation of glucose [56], can also generate acetic acid through isomerization/dehydrogenation pathways, or via an acetaldehyde intermediate [14,19,59]. Accordingly, the main liquid products identified and quantified are organic acids, namely lactic (LA), levulinic (LEA), propionic (PA), and acetic acids (AA) (Fig. 7). LA derives from firstly the isomerization of glucose to fructose, then the retro-aldol cleavage of fructose which leads to glyceraldehyde and dihydroxyacetone [14], followed by the rearrangement and dehydration steps leading to pyruvaldehyde, which is unstable in the reaction conditions, and then LA [60]. Isomerization and retro-aldol cleavage need both Lewis acid and basic sites over the catalyst's surface [59,61]. PA derives from the further hydrodeoxygenation of LA [62]. LEA, together with formic acid, is produced via rehydration of 5-hydroxymethylfurfural (HMF), formed by acid-catalysed dehydration of fructose. HMF further undergoes hydrolytic ring-opening through the reactive intermediate 2,5-dioxo-6-hydroxyhexanal (DHH), leading to levulinic acid and formic acid formation [63,64]. Formic acid was not quantified, as under the investigated reaction conditions it is rapidly reformed into H_2.

Although the mechanism of humin formation, which could lead to catalyst deactivation, is still under debate, HMF is widely recognized as a key intermediate in humin formation pathways [48,50]. In addition, glycolaldehyde, glyceraldehyde, pyruvaldehyde and DHH, which have been proposed as reaction intermediates in the mechanistic pathways leading to the identified liquid products, belong to the class of highly reactive α-carbonyl aldehydes and are suggested to contribute to humin formation via condensation reactions [49].

In the liquid phase, neither glucose nor other soluble sugars were detected in any of the tests, indicating their rapid consumption under the applied reaction conditions. Ni0 favoured the formation of lactic acid due to the acid–base properties of the catalyst surface, without a corresponding increase in hydrogen production. In contrast, the introduction of metallic Ni in Ni15 and Ni24 promoted the formation of levulinic acid (LEA), which is co-produced with formic acid, an intermediate that can subsequently contribute to H_2 formation via reforming reactions. The increased Lewis acidity in Ni-containing samples, as observed from TPD analysis performed on the Ni24 catalyst, may therefore account for the higher LEA formation observed., which requires acidic functionalities for the previous formation of HMF from fructose.

When Ni35 was used as catalyst, the product distribution resembled the one observed for Ni0, with lactic acid remaining the predominant liquid product and no substantial enhancement in hydrogen production. This behaviour suggests that the high Ni loading does not translate into improved catalytic activity. The pronounced loss of surface area and the aggregation of Ni during reduction, as evidenced by BET and XRD analyses likely results in decreased accessibility and effectiveness of the metallic active phase during APR.

Interestingly, CO chemisorption analyses (Table 2) revealed that Ni35 exhibited the highest amount of exposed metallic Ni sites and the highest apparent Ni dispersion among the investigated catalysts. Nevertheless, no direct proportionality was observed between the amount of exposed metallic sites and H_2 productivity. Despite its higher CO uptake, Ni35 displayed the lowest hydrogen productivity, whereas Ni24 exhibited the highest catalytic performance. These results indicate that catalytic activity is not governed solely by the amount of accessible metallic Ni sites, but rather by the combined effect of metallic site accessibility, textural properties, metal–support interaction, and acid–base functionalities. In this respect, Ni24 appears to provide the most favourable compromise among these properties, resulting in superior catalytic performance. This is also suggested by XPS results were the presence of Ni^{2+} on the surface together with metallic Ni is indicative of positive interaction between metal and support which favours the C–C and C–H bonds leading to higher hydrogen production [34].

Consequently, Ni35 behaves similarly to the Ni-free catalyst, although with lower overall activity. These findings confirm that an appropriate tuning of the Ni content is essential to ensure optimal catalytic performance.

Table 2
CO uptake, apparent Ni dispersion, and hydrogen productivity of the investigated NiMgAl catalysts. Hydrogen productivity values refer to the reaction conditions reported in Fig. 6.

Catalyst	CO uptake ($\mu mol_{CO}.g_{CAT}^{-1}$)	Ni dispersion (%)	H_2 productivity ($mmol_{H2}.g_{CAT}^{-1}.h^{-1}$)
Ni15	33.9	1.2	5.8
Ni24	42.1	1.1	8.0
Ni35	104.7	1.8	2.6

On this basis, Ni24 was selected as the reference catalyst for all subsequent catalytic tests.

3.2.2. Effect of substrate

The catalytic activity of Ni24 was evaluated using different substrates, namely glucose and cellulose pulp. The catalytic tests were carried out under identical conditions (250 °C, 3 h, 1.50 g of substrate, 0.45 g of catalyst, 1atm N_2 atmosphere). The corresponding yields of gaseous and main liquid products, together with the hydrogen productivity expressed as $mmol_{H2}.h^{-1}\cdot g_{CAT}^{-1}$ are reported in Fig. 8.

A markedly higher H_2 yield was obtained when cellulose was used as substrate (≈20%) compared to glucose (≈3%). This result is unexpected, as more complex feedstocks generally lead to lower hydrogen selectivity [11,65].

As reported by Bensaid et al. [66], this behaviour can be ascribed to the tendency of glucose to undergo polymerization at high concentrations, which suppresses H_2 selectivity during the aqueous-phase reforming (APR) process. Elevated glucose concentrations favour intermolecular condensation reactions, resulting in polymeric species that are inactive toward reforming, while hydrogen can be produced if the glucose concentration is reduced. In contrast, during APR of cellulose, the substrate first undergoes hydrolysis to glucose, which is then promptly converted into smaller molecules. Owing to the highly active redox nature of the metallic phase and the ability of the mixed oxide support to promote gradual hydrolysis, the glucose concentration remains low throughout the reaction. This continuous in situ consumption limits polymerization pathways and enhances hydrogen production.

3.2.3. Effect of reaction time and mechanism of reaction

The effect of reaction time on the performance of the Ni24 catalyst was investigated by conducting experiments using cellulose pulp as substrate with reaction time ranging from 1 to 4 h. The catalytic tests were carried out at 250 °C, charging 1.50 g of cellulose and 0.45 of catalyst, in 1 atm N_2 atmosphere. The resulting distributions of gaseous products, together with the hydrogen productivity expressed as $mmol_{H2}\cdot h^{-1}\cdot g_{CAT}^{-1}$, and liquid products are reported in Figs. 9 and 10, respectively.

Regarding the gas phase, all tests showed the formation of H_2 and CO_2 as the main products, with overall similar trends for both species, consistent with the occurrence of the water–gas shift (WGS) reaction. Carbon monoxide was not detected, most likely due to its rapid in situ conversion via WGS under the applied reaction conditions. At 4 h of

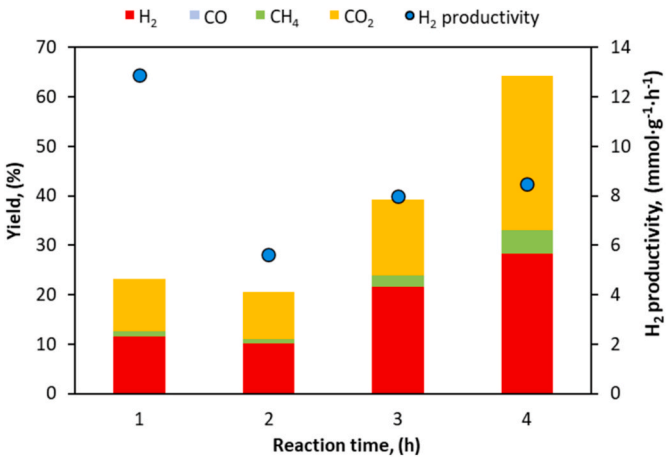

Fig. 9. Effect of the reaction time on the yield of the gaseous products and H_2 productivity during APR of cellulose on the Ni24 catalyst. 250 °C, 1.5 g cellulose, 0.45 g cat., 50 mL water, 1,2,3 and 4 h, N_2 atm.

reaction time, CO_2 was obtained in slightly higher yield (31%) than H_2 (28%). This difference likely arises from the progressive contribution of hydrogenation reactions at longer reaction times, which consume part of the produced hydrogen, leading to a lower net H_2 yield. Minor amounts of CH_4 were also detected, probably originating from methanation reactions. (Fig. 8).

Hydrogen productivity exhibited a non-monotonic trend with reaction time. It was relatively high at 1 h, partly due to the short reaction time used in its calculation, then decreased at 2 h, suggesting the onset of competitive hydrogenation reactions that temporarily consume part of the formed H_2. Between 3 and 4 h, hydrogen productivity increased again, indicating a greater contribution of reforming-dominated pathways leading to H_2 formation. Beyond 4 h, productivity levelled off at approximately 8.5 mmol H_2 $g_{CAT}^{-1}\cdot h^{-1}$, suggesting that prolonged reaction times progressively favour hydrogen-consuming reactions and provide limited additional benefit. Overall, 3 h represents a reasonable compromise under the investigated conditions.

The liquid-phase product yields are reported in Fig. 10. Lactic acid was detected in all tests, but its yield progressively decreased with reaction time, from 13.5% at 1 h to 1.9% at 4 h. In contrast, propionic acid followed the opposite trend, increasing from 1.1% to 6.7%, suggesting

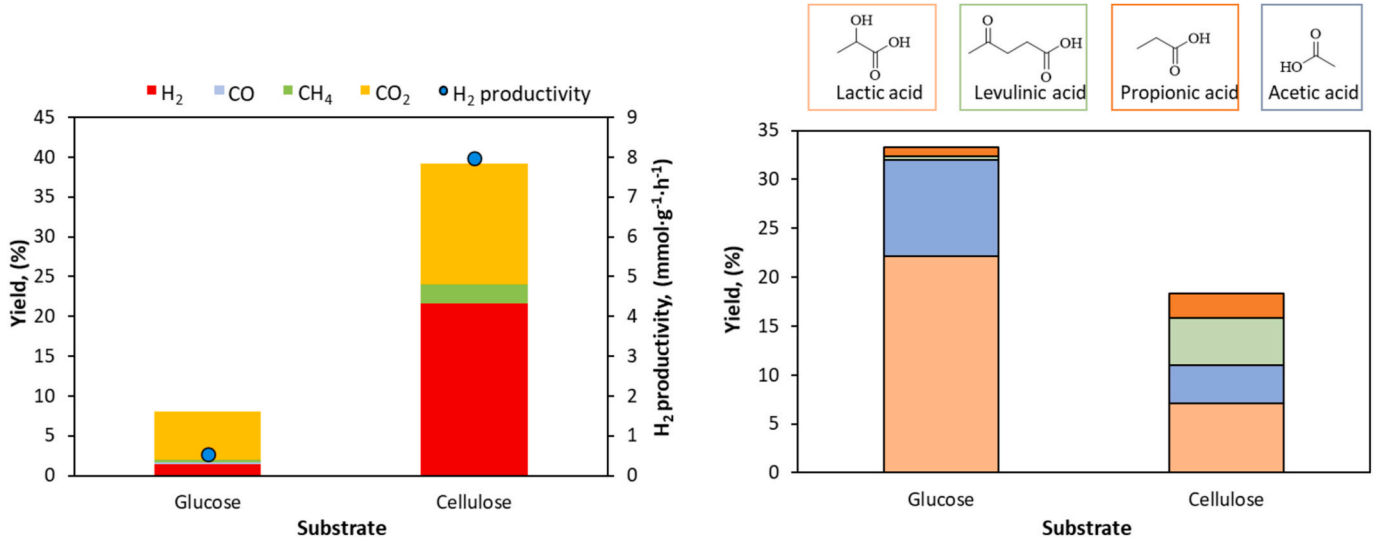

Fig. 8. Effect of the substrate on over the products yields with Ni24 as catalyst. 250 °C, 1.5 g subst. 0.45 g cat., 50 mL water, 3 h, N_2 atm. On the left the yields of gaseous products and H_2 productivity, on the right the yields of the main liquid products.

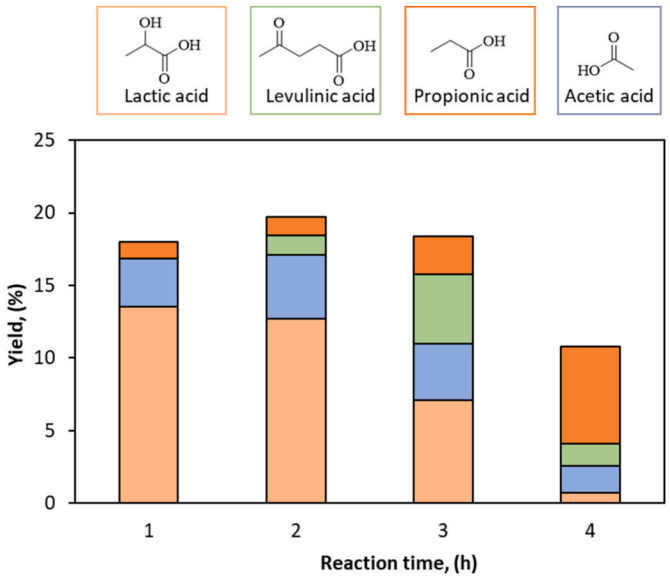

Fig. 10. Effect of the reaction time on over the main liquid products distribution during APR of cellulose on the Ni24 catalyst. 250 °C, 1.5 g cellulose, 0.45 g cat., 50 mL water, 1,2,3 and 4 h, N_2 atm.

that longer reaction times promote the hydrodeoxygenation of lactic acid to propionic acid with concurrent hydrogen consumption, consistent with the hydrogen yield trend observed in Fig. 9. Levulinic acid increased between 2 and 3 h (up to ~5%), then decreased at longer times, likely due to further conversion. Acetic acid was detected in all tests, with a yield of about 4% during the first 3 h, decreasing to 1.9% at 4 h. This behaviour may be rationalized considering that acetic acid can originate from the dehydrogenation of ethylene glycol, which in turn derives from hydrogenation of glycolaldehyde. If lactic acid hydrodeoxygenation is kinetically favoured at longer times, it may compete more effectively for the available hydrogen, thereby limiting glyceraldehyde hydrogenation to ethylene glycol. This would reduce acetic acid formation and is consistent with the plateau observed in hydrogen productivity.

To identify intermediates of the reaction mechanism we have performed a reaction at a lower temperature (200 °C) and without the reforming active phase (Ni0 catalyst) for 3 h. The reaction yielded glucose (7% yield), fructose (4%), lactic acid (16%), formic acid (10%), ethylene glycol (2%) and acetic acid (7%) showing that the mechanism passes through the hydrolysis to sugars and then to retro-aldol condensations.

Based on the observed product distribution in both the gas and liquid phases, together with literature data the reaction network can be rationalized in terms of three main reaction pathways starting from the cellulose hydrolysis product, glucose, schematically illustrated in Fig. 11, each exerting a different influence on hydrogen production.

The first pathway involves the isomerization of glucose to fructose, followed by retro-aldol cleavage to yield C_3 intermediates such as glyceraldehyde and dihydroxyacetone. These species can undergo subsequent dehydration and rearrangement reactions to form organic acids, including lactic acid, which may further convert to propionic acid via hydrodeoxygenation under reductive conditions. A key intermediate of this pathway is pyruvaldehyde, as depicted in Fig. 11 which can lead to the formation of lactic acid, which then leads to further products. To assess this hypothesis a test under a hydrogen atmosphere using the Ni24 catalyst and pyruvaldehyde as a reagent was carried out, showing that the reaction produces lactic acid and propionic acid by dehydration and subsequent hydrogenation.

The second pathway also originates from fructose and proceeds through its dehydration to 5-hydroxymethylfurfural (HMF). Subsequent rehydration of HMF leads to the formation of levulinic acid and formic acid. The latter can indirectly contribute to hydrogen production through decomposition and reforming reactions. Formic acid was also tested under a nitrogen atmosphere for 3 h using Ni24 and showed total conversion toward hydrogen and carbon dioxide, indicating it as one of the desired hydrolysis/retro aldol condensation products.

The third pathway is associated with the reforming and hydrogenolysis of short-chain oxygenated compounds, including ethylene glycol and ethanol, which promote hydrogen generation without

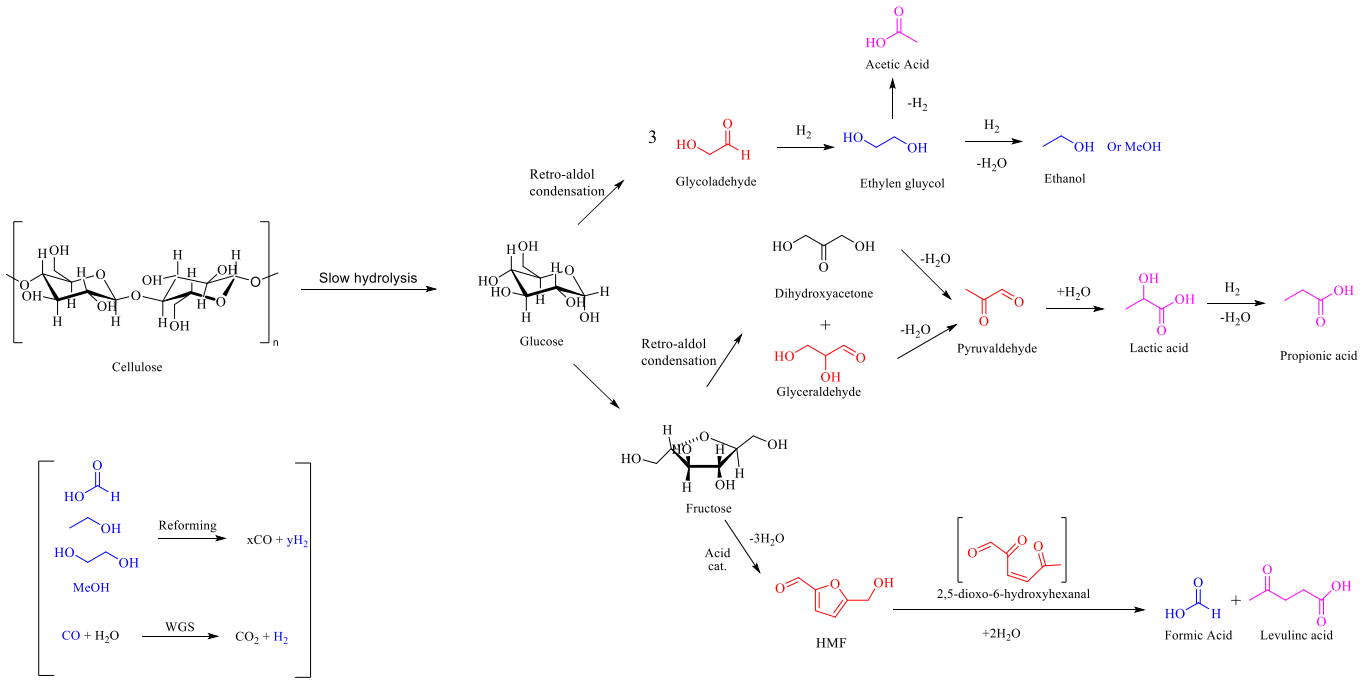

Fig. 11. Proposed mechanism of cellulose APR on NiMgAl catalyst. Red: products leading to humins; Blue: products leading to H_2; Purple: products not leading to H_2. (For interpretation of the references to colour in this figure legend, the reader is referred to the Web version of this article.)

significant accumulation of stable liquid by-products. Ethylene glycol derives from the hydrogenation of glycolaldehyde, which is formed by the retro-aldol condensation of glucose. This was also confirmed by conducting a test with glycolaldehyde for 3 h in a hydrogen atmosphere using Ni24, which led to the production of ethylene glycol, acetic acid and mainly ethanol. In addition, a reaction was conducted under nitrogen with ethylene glycol as reagent to show their conversion to hydrogen (75% yield) and CO_2 (41%). The reaction showed an almost complete conversion of the reagent, co-producing low amounts of ethanol and methanol. Given that ethylene glycol and its hydrogenation product, ethanol, are easily reformable products under these reaction conditions using Ni and Pt-based catalysts as shown by this test, this pathway becomes the most preferable one for hydrogen production and the use of catalysts like Ni or Pt, which are not only able to catalyse reforming but also hydrogenations is of fundamental importance.

This mechanism is simplified due to identification of only the most important products because of the complexity of the reaction system and in particular the following pathways has been identified by this study: hydrolysis of cellulose to glucose, glycolaldehyde conversion to ethylene glycol ethanol and acetic acid, the conversion of the ethylene glycol to hydrogen, ethanol and methanol, the conversion of pyruvaldehyde to lactic and propionic acid and the conversion of formic acid to hydrogen. On the other hand, in the HMF pathway, the production of glycolaldehyde or pyruvaldehyde from fructose is speculated based on literature results [14,19,45,48–50,59–61,63,67–70] Nevertheless, Fig. 11 allows to draw indications on how to push toward hydrogen production in reactions involving cellulose, glucose, fructose, or some of their derivatives.

In fact, the observed variation in hydrogen yield with reaction time suggests that H_2 formation is governed by the relative balance between reforming-dominated and hydrogen-consuming pathways. In particular, pathways involving intermediates such as ethylene glycol appear to play a key role, as they promote hydrogen production without necessarily leading to the accumulation of stable liquid products. In this context, introducing hydrogen in the initial reaction atmosphere may facilitate the hydrogenolysis of glucose-derived intermediates and enhance subsequent reforming reactions, thereby accelerating the establishment of hydrogen-producing routes and improving overall hydrogen formation.

3.2.4. Effect of the reaction atmosphere (H_2) on cellulose APR

3.2.4.1. Effect of H_2 presence. The effect of the reaction atmosphere on the APR of cellulose was investigated using Ni24 as catalyst by performing experiments under different initial gas compositions. Before Prior to the reaction, the autoclave was charged at room temperature (r.t.) with 1 atm of N_2, 1 atm of pure H_2, or 2.1 atm of pure H_2. All catalytic tests were carried out at 250 °C for 3 h, loading 1.50 g of cellulose pulp and 0.45 g of catalyst, so given the higher temperature and the autogenous pressure conditions, the hydrogen pressure increased thanks to the increase in total pressure. The resulting hydrogen yields and product distributions together with the hydrogen productivity expressed as $mmol_{H2}\, g_{CAT}^{-1}\, h^{-1}$, are reported in Fig. 12.

A remarkable enhancement in hydrogen production was observed in the presence of H_2. In particular, it was possible to reach a maximum value of hydrogen yield of approximately 40% in the presence of 1 atm (at room temperature) of pure H_2. Although counterintuitive, given that hydrogen is both introduced and produced during the reaction, this result highlights the crucial role of a reductive reaction environment in promoting hydrogen-forming pathways. Conversely, increasing the hydrogen pressure to 2.1 atm resulted in a decrease in hydrogen yield, suggesting that excessively high H_2 partial pressures favour hydrogenation reactions at the expense of net hydrogen production. These three tests allowed to investigate the effect of hydrogen partial pressure and at similar total pressure and water vaporization in autogenous conditions on the catalytic activity as the partial pressure of hydrogen increased from 0 (under nitrogen atmosphere) to 1.8 atm at 250 °C (for the test with 1 atm of hydrogen loaded at r.t.) to 3.70 at 250 °C (for the test with 2.1 atm of hydrogen loaded at r.t.). This did not lead to a high increase in total pressure developed in autogenous conditions which were between 40 and 41 atm throughout all the three tests. The addition of hydrogen at 2.1 atm decreased the contribution of water that was vaporised at 250 °C, from 4.8% of the total water amount to 4.3%.

The presence of H_2 likely accelerates the hydrogenolysis of cellulose and hydrogenation of cellulose-derived intermediates, thereby favouring reaction routes that enhance hydrogen formation. In particular, APR pathways involving ethylene glycol require an initial hydrogenation step, as this molecule is formed through the reduction of glycolaldehyde. Subsequent reforming of ethylene glycol (Eq. (6)) and of its

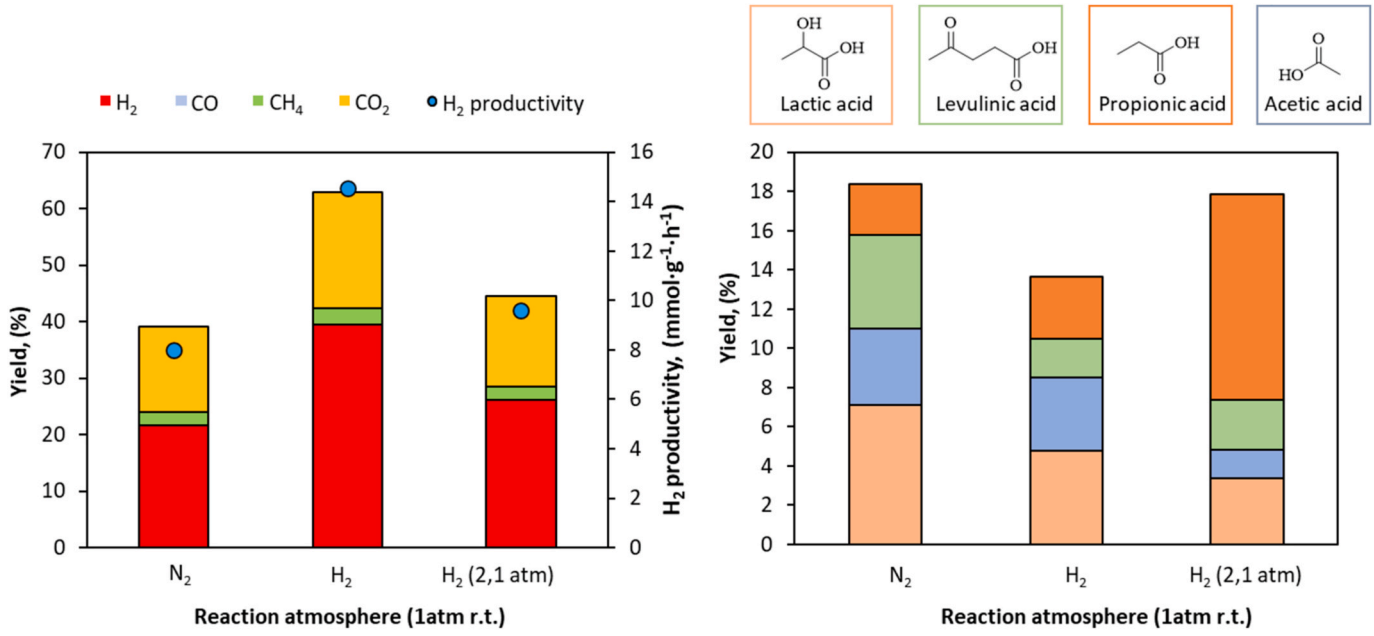

Fig. 12. Effect of the reaction atmosphere on over the yields of gaseous and liquid products and H_2 productivity during APR of cellulose on the Ni24 catalyst. 250 °C, 1.5 g cellulose, 0.45 g cat., 50 mL water, 3 h, 1 atm N_2, 1 atm H_2 and 2.1 atm H_2.

hydrogenation product, ethanol (Eq. (7)), leads to additional hydrogen generation, stoichiometrically providing more hydrogen than the one consumed. Moreover, molecular hydrogen can promote the direct hydrogenolysis of cellulose toward ethylene glycol and other short-chain oxygenated intermediates, which can then undergo reforming reactions.

$$C_2H_6O_{2(l)} + 2H_2O_{(l)} \rightleftharpoons 2CO_{2_{(g)}} + 5H_{2_{(g)}} \quad \text{(Eq. 6)}$$

$$CH_3CH_2OH_{(l)} + 3H_2O_{(l)} \rightleftharpoons 2CO_{2_{(g)}} + 6H_{2_{(g)}} \quad \text{(Eq.7)}$$

In addition, H_2 can be partially consumed in the reduction of carbonyl groups of aldehydes and ketones, such as dihydroxyacetone, glyceraldehyde, pyruvaldehyde, and glycolaldehyde (see the reaction scheme in Fig. 11), thereby reducing condensation reactions leading to humin formation. By inhibiting these undesired polymerization pathways, the presence of H_2 increases the availability of reformable intermediates and helps maintain the metallic Ni phase in its reduced state throughout the reaction. To confirm this, the carbon balances of the reactions were closed to compare the amount of gaseous (mainly carbon dioxide and methane) liquid and solid carbon. In particular, in the case of the test carried out in a nitrogen atmosphere 17% of carbon was converted into gaseous products, while 43% was found as soluble products and the remaining 40% as solid. By adding hydrogen, the proportion changed with 23% of carbon in gas phase, 39% in liquid phase and 38% as solid. This shows how the addition of hydrogen increases the reaction pathways to gaseous products, which are obtained from hydrogen generating reactions (i.e. CO_2 by water gas shift reaction), thanks to a slight reduction in the humins formation.

Nevertheless, the relatively limited difference between the two conditions also suggests that humin formation remains a significant competing pathway even under H_2 atmosphere.

ATR-IR analysis was used to characterize the humins formed over the catalysts under nitrogen or hydrogen. Interestingly, the bands related to C═O and C═C were less intense for the test carried out with hydrogen addition, which suggests that its presence favoured the reduction of C═C and C═O double bonds (Fig. S13).

Analysis of the liquid-phase products (Fig. 12) indicates that changes in the reaction atmosphere do not markedly alter the overall product distribution. However, in the experiment carried out under 2.1 atm of H_2, a higher concentration of propionic acid was detected, which results from the hydrodeoxygenation of lactic acid, further supporting the hypothesis that elevated H_2 pressure promotes hydrogenation reactions, ultimately reducing hydrogen yield, further supporting the hypothesis that elevated H_2 pressure promotes hydrogenation reactions, ultimately reducing hydrogen yield.

3.2.4.2. Effect of reaction time under H_2 atmosphere on cellulose APR. To further investigate the effect of an initial H_2 atmosphere on cellulose APR, in this section the presence of hydrogen has been analysed at different reaction times (2, 3, and 4 h) and compared with results obtained under an N_2 atmosphere, using Ni24 as the catalyst. All catalytic tests were carried out at 250 °C, loading 1.50 g of cellulose pulp and 0.45 g of catalyst, under 1 atm of either N_2 or H_2. The results are depicted in Figs. 13 and 14.

As shown in Fig. 13, the presence of H_2 in the reaction atmosphere may promote both the hydrogenolysis of cellulose-derived intermediates and the subsequent reforming reactions, leading to enhanced hydrogen formation. Under an H_2 atmosphere, the maximum hydrogen productivity was reached already after 2 h of reaction (14.5 mmol•g_{CAT}^{-1}·h^{-1}), whereas under N_2 atmosphere the maximum value was attained only after 3 h. This behaviour suggests that the initial presence of hydrogen accelerates reductive intermediate steps involved in the reaction network, which subsequently favour H_2 production. For instance, glycolaldehyde can be hydrogenated to ethylene glycol, which may undergo further hydrogenation to ethanol; both ethylene glycol and ethanol are readily converted through reforming pathways, contributing to additional hydrogen formation (see proposed mechanism in Fig. 10). In contrast, when N_2 is used, hydrogen must first be generated in situ before these pathways become predominant. Nevertheless, prolonged reaction times may still favour competitive hydrogen-consuming reactions, limiting the net H_2 productivity. The availability of molecular hydrogen likely facilitates the conversion of reactive oxygenated intermediates into short-chain species that are readily reformed, thus promoting faster activation of hydrogen-producing pathways. These results indicate that H_2 does not simply act as an inert component of the reaction atmosphere, but actively contributes to shifting the reaction network toward hydrogen formation, enabling the system to reach its maximum productivity at shorter reaction time. In fact, Dumesic and coworkers had shown that reducing sugars to polyols before APR increased the overall hydrogen formation decreasing humin formation. However, in their system hydrogenation was carried out in a separate reactor, followed by APR an inert atmosphere. This work shows how the use of a reducing agent can be applied directly to the APR reactor, intensifying the process and opening the way for the use of reductive atmospheres in APR [71].

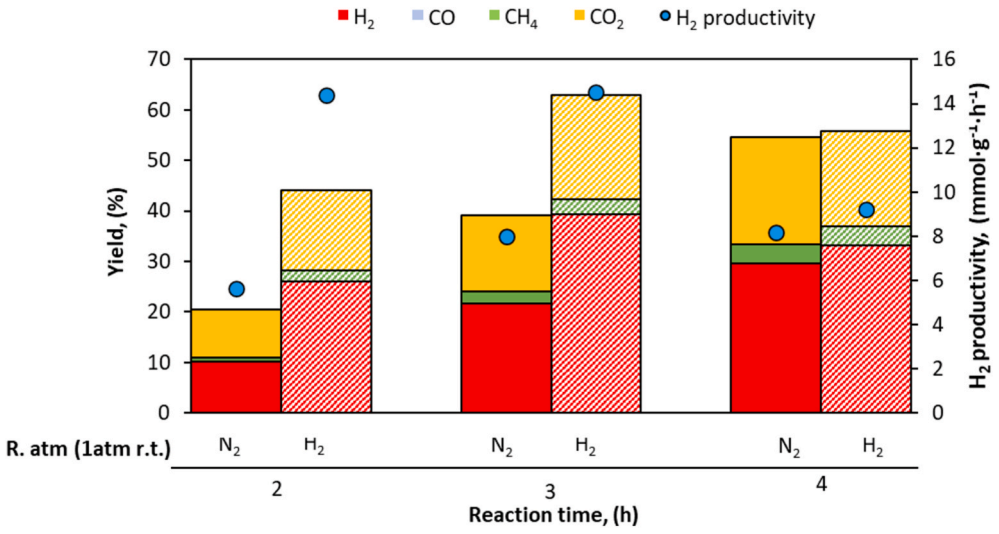

Fig. 13. Effect of the reaction time over the yields of gaseous products and H_2 productivity during APR of cellulose on the Ni24 catalyst with different reaction atmosphere. 250 °C, 1.5 g cellulose. 0.45 g cat., 50 mL water, 2, 3 and 4 h,1 atm N_2 or H_2.

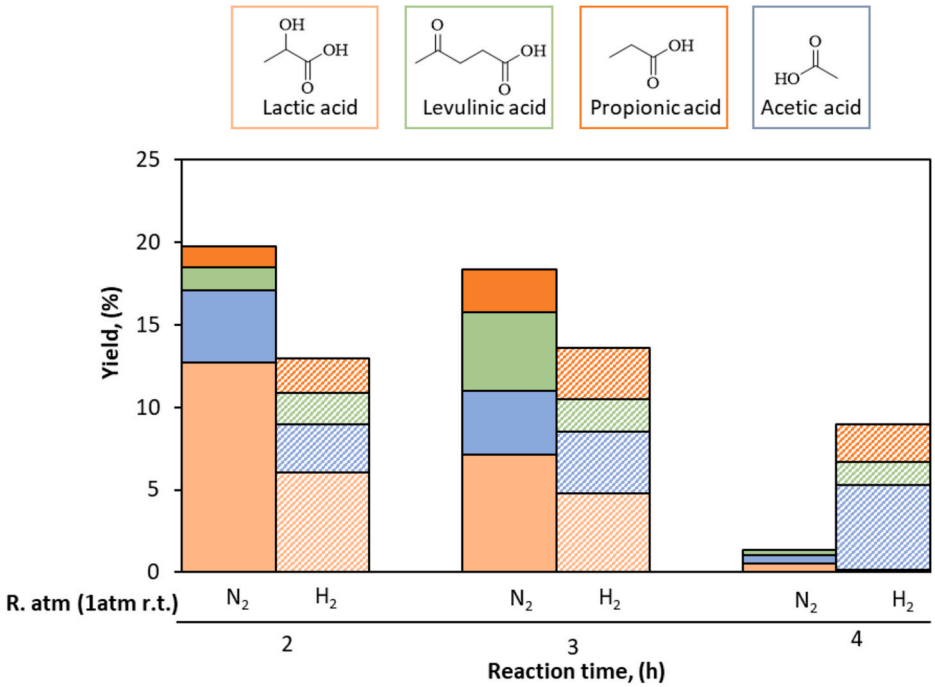

Fig. 14. Effect of the reaction time over the yields of the main liquid products during APR of cellulose on the Ni24 catalyst. 250 °C, 1.5 g cellulose. 0.45 g cat., 50 mL water, 2, 3 and 4 h, N_2 or H_2 atm.

3.2.5. *Recycle test and used catalyst characterization*

To assess the effect of prolonged reaction time over the Ni24 catalyst, three tests were performed repeatedly at 250 °C, 3 h and nitrogen atmosphere recovering by filtration the catalyst and just drying it before the following test. The results, depicted in Table 3, show that the catalyst undergoes deactivation throughout time. To assess the causes of this deactivation different analysis were carried out. First of all, ICP was conducted on the liquid phases collected after APR reaction. Ni concentrations were determined using the emission lines at 341.47, 352.45, and 361.93 nm. The measured Ni leaching corresponded to 0.4% of the initial Ni content indicating limited metal leaching under the investigated reaction conditions, which thus is not the cause of deactivation. XRD analysis of the used catalyst was also carried out. The used Ni24 catalyst after 3 h under nitrogen was analysed by XRD to probe the structural evolution of the oxide and eventual oxidation of Ni particles, by IR and Raman to analyse the presence of humins and carbonaceous deposits, by nitrogen physisorption to quantify eventual loss of surface area.

The XRD analysis (Fig. 15) shows the reconstruction of the layered double hydroxide phase after hydrothermal treatment of the oxide during the reaction, which may cause surface area decrease, though keeping acid-base properties typical for these materials [72]. In addition, the presence of metallic Ni phase was observed, indicating the preservation of active metal sites during the hydrothermal conditions of the first test. The average crystallite sizes were kept at around 15 nm (compared to 14 recorded by the fresh sample) indicating that sintering did not occur during the first test regardless of the hydrothermal conditions and the phase change of the mixed oxide. However, the used catalysts analysed after the three tests did not show the presence of any Ni phase, suggesting a total oxidation of this metallic phase. The

Table 3
Results of the gas phase of recycling test performed by using Ni24 sample under H2 atmosphere.

	1st test	1st recycle	2nd Recycle
H_2 Yield (%)	21	10	4

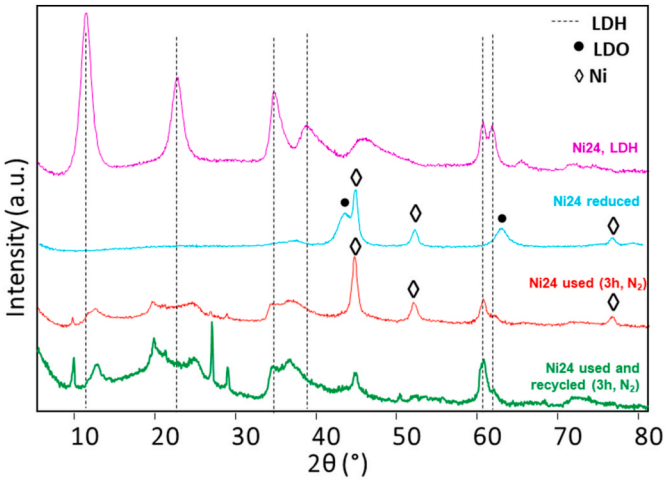

Fig. 15. XRD patterns of the Ni24 catalyst at different stages: LDH precursor (purple), calcined and reduced catalyst (light blue), spent catalyst after the first APR cycle (red), and spent catalyst after the second APR recycle (green). Reaction conditions: 250 °C, 1.5 g cellulose, 0.45 g catalyst, 50 mL water, 3 h, 1 atm N_2 atmosphere. (For interpretation of the references to colour in this figure legend, the reader is referred to the Web version of this article.)

presence of carbon-based deposits over the sample was probed by ATR-IR analysis which showed the presence of additional bands in comparison with the fresh sample (see Fig. 16).

The absorption bands at approximately 2920 cm^{-1} and 2850 cm^{-1} are attributed to the asymmetric and symmetric C–H stretching vibrations, respectively, associated with aliphatic hydrocarbons. A prominent peak around 1730 cm^{-1} suggests the presence of carbonyl groups (C═O) from esters, ketones, or carboxylic acids. The peaks around 1400 cm^{-1} can be attributed to the C–C stretching of aromatic compounds. The peaks centred around 1050 cm^{-1} can be ascribed to C–O stretching vibrations of alcohols, esters, and carboxylic acids. The fresh catalyst only exhibits the existence of M − O bonds at 460–600 cm^{-1}. These results

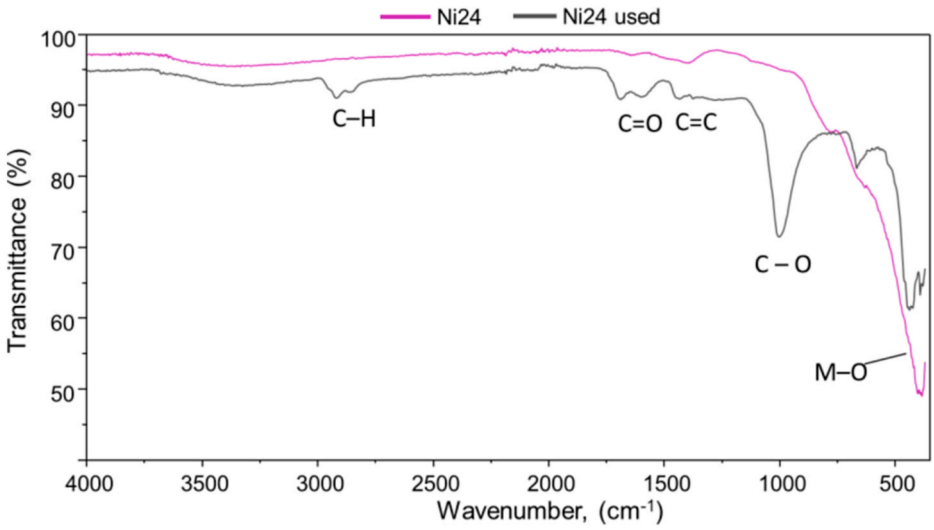

Fig. 16. ATR-IR spectra of the fresh reduced Ni24 catalyst (purple) and the spent Ni24 catalyst recovered after the second APR cycle (green). Reaction conditions: 250 °C, 1.5 g cellulose, 0.45 g catalyst, 50 mL water, 3 h, 1 atm N_2 atmosphere. (For interpretation of the references to colour in this figure legend, the reader is referred to the Web version of this article.)

show that humins are deposited over the catalyst which removes the active phase from the reaction environment contributing to deactivation and performance loss. As the reconstruction to LDH and the formation of humins may lead to decrease of surface area nitrogen physisorption was conducted. The analysis of the fresh sample and of the samples after one and three reaction tests has shown a decrease of the surface area due to the deposition of carbon compounds and phase reconstruction, as it is possible to see from Table 4. The formation of humins, the oxidation of Ni and the decrease of surface area are spotted as the causes of performance loss under repeated tests.

Given the high initial activity of the Ni24 sample, further studies will concentrate on methods to increase its stability. In particular, submitting the recovered catalyst to calcination and reduction (which restores the mixed oxide and Ni nanoparticles) has been already reported to provide stable results [34]. However, this implies regenerating the catalyst after each step and for this reason future research will focus on finding strategies to avoid the deactivation phenomena, for instance by adding stability promoters, increasing mechanical stability or adding additional active phases able to reduce humin formation pathways, as well as operating on reaction conditions. For instance, active phases able to work at lower temperature and produce significant cellulose hydrolysis and hydrogen under those conditions, would allow to slow down humin formation, which is less favoured below 200 °C.

3.2.6. Comparison of catalyst performance with state-of-art systems on cellulose APR

Pt is one of the most studied metals employed as heterogeneous supported catalysts for the APR of biomass-derived oxygenated compounds, and is commonly reported among the most active systems for this reaction [11,13,23]. Here, the catalytic performance of the most promising NiMgAl-LDH-derived catalyst (Ni24) was compared with that of a Pt/Al_2O_3 catalyst prepared in the laboratory, as described in the Materials and Methods section. Catalytic tests were carried out under identical reaction conditions (250 °C, 3 h, 1.50 g cellulose pulp, 0.45 g catalyst, 50 mL water, 1 atm N_2 atmosphere), and the results are reported in Fig. 17.

Table 4
Surface area of the sample on fresh and spent Ni24 catalyst.

Sample	Surface Area (m^2*g^{-1})
Ni24 fresh reduced	90
Ni24 after 1 test	52
Ni24 after 3 tests	6

As observed, under identical reaction conditions the Ni24 catalyst achieved a significantly higher hydrogen productivity than Pt/Al_2O_3 (≈8 vs ≈ 4 $mmol_{H2}·g_{CAT}^{-1}·h^{-1}$). Moreover, analysis of the liquid phase reveals the presence of levulinic acid when Ni24 is used as catalyst. The formation of levulinic acid can be associated with enhanced hydrogen production, as it is generated through the rehydration of HMF, which simultaneously yields formic acid, a hydrogen source. Subsequent decomposition/reforming of formic acid contributes directly to additional H_2 formation.

To provide a more rigorous comparison between the two catalytic systems, hydrogen productivity was also normalized both to the total amount of metal and to the amount of exposed metallic sites estimated by CO chemisorption. The corresponding results are reported in Table 5. When normalized to the total metal amount, Pt/Al_2O_3 exhibited a substantially higher hydrogen production rate (27.90 $mmol_{H2}·mmol_{METAL}^{-1}·h^{-1}$) than Ni24 (1.68 $mmol_{H2}·mmol_{METAL}^{-1}·h^{-1}$) owing to its lower metal loading and its higher dispersion in respect to Ni24. However, the turnover frequency (TOF) values calculated from the exposed metallic sites resulted in 0.053 s^{-1} for Ni24 and 0.038 s^{-1} for Pt/Al_2O_3, indicating that the Ni24 catalyst exhibits a slightly higher intrinsic activity under the investigated conditions when normalized to the accessible surface metal sites. These results indicate that, despite the lower intrinsic activity generally associated with Ni compared to noble metals, the proper tuning of the NiMgAl LDH-derived catalyst composition allows the development of a noble-metal-free catalytic system capable of achieving high hydrogen productivity under mild APR conditions using a real waste-derived cellulose feedstock.

4. Conclusion

This study demonstrates that aqueous-phase reforming of cellulose can be effectively tailored toward sustainable hydrogen production by combining hydrotalcite-derived NiMgAl catalysts with optimized reaction conditions. The use of waste-derived cellulose from the paper industry highlights the strong potential of this approach within a waste-to-hydrogen and circular economy framework. Among the investigated catalysts, the $Ni_{24}Mg_{56}Al_{20}$ emerged as the most effective formulation, offering an optimal balance between nickel loading, metal dispersion, and textural properties. The catalytic results indicate that hydrogen production is primarily governed by the availability and dispersion of

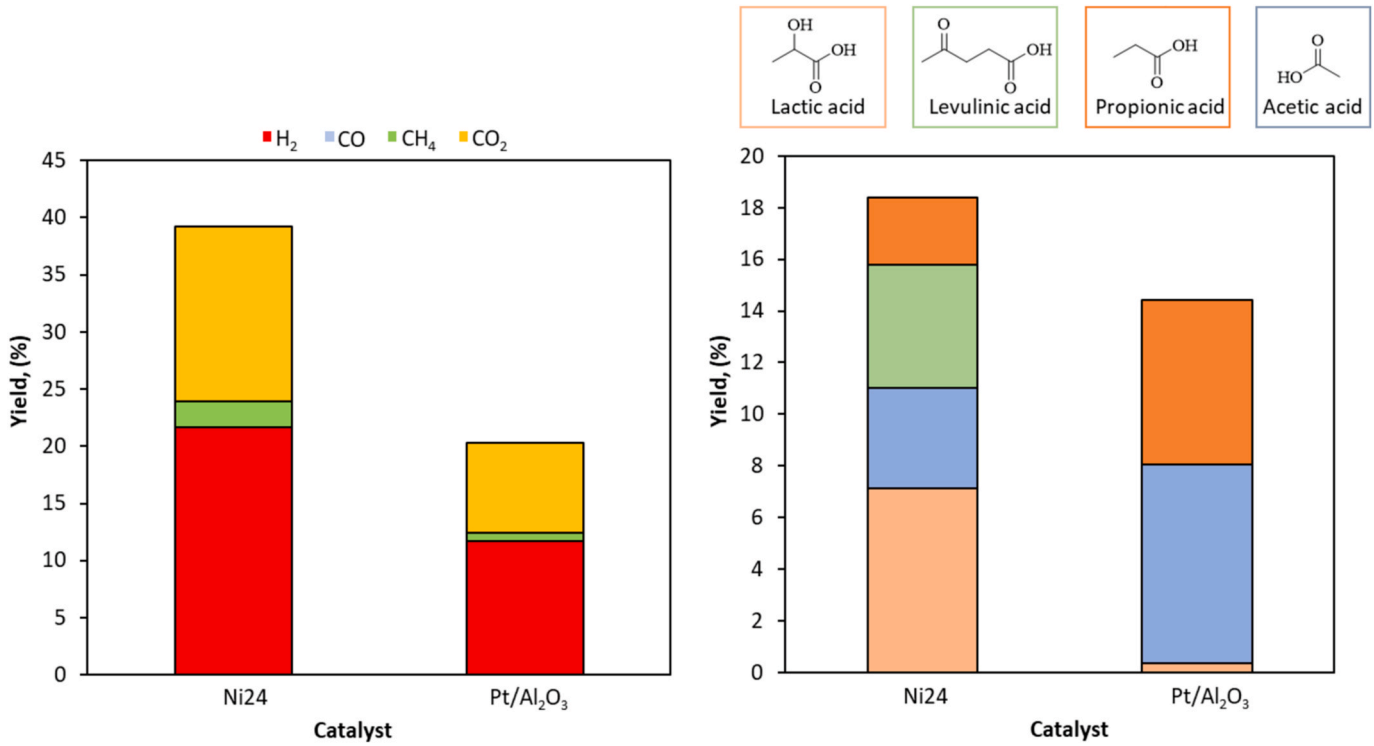

Fig. 17. Gaseous and main liquid products yields and H2 productivity during APR of cellulose over Ni24 and Pt/Al_2O_3 catalysts. 250 °C, 1.5 g cellulose. 0.45 g cat., 50 mL water, 3 h, 1 atm N_2.

Table 5
Comparison of hydrogen productivity, hydrogen productivity normalized to the total metal amount, CO uptake, and turnover frequency (TOF) for Ni24 and Pt/Al_2O_3 catalysts under the reaction conditions reported in Fig. 17. TOF values were calculated by normalizing the hydrogen production rate to the amount of exposed metallic sites estimated by CO chemisorption, assuming a CO/metal surface stoichiometry of 1:1.

Catalyst	H_2productivity		CO uptake	TOF
	$mmolH_2 \cdot g_{CAT}^{-1} \cdot h^{-1}$	$mmol_{H2} \cdot mmol_{MET}^{-1} \cdot h^{-1}$	$\mu mol_{CO} \cdot g_{CAT}$	s^{-1}
Ni24	7.98	1.68	42.06	0.053
Pt/Al_2O_3	4.29	27.90	31.11	0.038

metallic Ni. The study of the obtained products in both the gaseous and liquid phases allowed us to propose a reaction mechanism indicating that the main reaction pathways consist of both dehydration and hydrogenation/dehydrogenation pathways.

A key and counterintuitive finding of this work is the positive role of an initial H_2 atmosphere. Moderate H_2 addition markedly enhances hydrogen yields, reaching values as high as 40%, by promoting hydrogenolysis and reforming pathways while suppressing condensation reactions leading to humin formation. Conversely, excessive H_2 partial pressure favours hydrogenation reactions, ultimately reducing net hydrogen production. These results underline the critical role of the reaction atmosphere in directing APR reaction networks.

When compared with a state-of-the-art Pt/Al_2O_3 catalyst under identical conditions, the $Ni_{24}Mg_{56}Al_{20}$ catalyst exhibited apparent higher hydrogen productivity per gram of catalyst but also slightly higher turnover frequency values when normalized to the amount of exposed metallic sites estimated by CO chemisorption. In addition, the Ni-containing catalyst showed a product distribution characterized by higher levulinic acid formation, suggesting a greater contribution of reaction pathways involving HMF rehydration and formic acid generation, which may further contribute to hydrogen production Although Pt exhibited higher hydrogen productivity when normalized to the total metal amount, the results demonstrate that properly designed LDH-derived NiMgAl catalysts can represent promising noble-metal-free systems for hydrogen production from biomass-derived feedstocks under mild APR conditions. Overall, this work demonstrates that properly designed LDH-derived NiMgAl catalysts, combined with controlled reaction atmospheres, represent a cost-effective and sustainable alternative to noble-metal systems for hydrogen production from biomass and industrial waste streams. Further studies are needed to optimize catalyst composition and assess long-term stability, in order to fully exploit the potential of LDH-derived NiMgAl systems for sustainable hydrogen production.

CRediT authorship contribution statement

Emanuele Bosetti: Conceptualization, Data curation, Formal analysis, Investigation, Methodology, Validation, Visualization. **Giulia Balestra:** Conceptualization, Data curation, Formal analysis, Methodology, Validation, Visualization, Writing – original draft, Writing – review & editing. **Jacopo De Maron:** Conceptualization, Formal analysis, Methodology, Supervision, Validation. **Eleonora Tosi Brandi:** Data curation, Methodology, Validation, Visualization. **Andrea Fasolini:** Conceptualization, Data curation, Formal analysis, Investigation, Methodology, Supervision, Validation, Visualization, Writing – original draft, Writing – review & editing. **Francesco Basile:** Conceptualization, Formal analysis, Funding acquisition, Methodology, Project administration, Resources, Supervision, Validation.

Declaration of competing interest

The authors declare the following financial interests/personal relationships which may be considered as potential competing interests: Francesco Basile reports financial support was provided by European Union. If there are other authors, they declare that they have no known competing financial interests or personal relationships that could have appeared to influence the work reported in this paper.

Appendix ASupplementary data

Supplementary data to this article can be found online at https://doi.org/10.1016/j.ijhydene.2026.156400.

References

[1] Ozkan C, Susanlı ZB, Okay N. Energies 2025;18.
[2] Fan Z. Highlights Sci Eng Technol 2024;116:237–40.
[3] Handique AJ, Peer R, Haas J, Osorio-Aravena JC, Reyes-Chamorro L. Int J Hydrogen Energy 2024;85:427–39.
[4] Abawalo M, Pikoń K, Landrat M, Ścierski W. Energies 2025;18.
[5] Kapdan IK, Kargi F. Enzym Microb Technol 2006;38:569–82.
[6] Demirbas A. Energy Convers Manag 2008;49:2106–16.
[7] Aziz M, Darmawan A, Juangsa FB. Int J Hydrogen Energy 2021;46:33756–81.
[8] Fasolini A, Cespi D, Tabanelli T, Cucciniello R, Cavani F. Catalysts 2019;9.
[9] Ni M, Leung DYC, Leung MKH, Sumathy K. Fuel Process Technol 2006;87:461–72.
[10] Oliveira AS, Baeza JA, Calvo L, Gilarranz MA. Chem Eng J 2023;460:141770.
[11] Cortright RD, Davda RR, Dumesic JA. Nature 2002;418:964–7.
[12] Chheda JN, Huber GW, Dumesic JA. Angew Chem Int Ed 2007;46:7164–83.
[13] Shabaker JW, Davda RR, Huber GW, Cortright RD, Dumesic JA. J Catal 2003;215:344–52.
[14] Lv J, Meng X-G, Huang H, Wang F, Yu W-W, Wu Y-Y. Catal Commun 2020;145:106098.
[15] Fasolini A, Cucciniello R, Paone E, Mauriello F, Tabanelli T. Catalysts 2019;9.
[16] Joshi AN, Vaidya PD. Int J Hydrogen Energy 2024;49:117–37.
[17] Rosmini C, Urrea MP, Tusini E, Indris S, Kovacheva D, Karashanova D, Kolev H, Zimina A, Grunwaldt J-D, Rønning M, Dimitrov M, Popova M. Appl Catal B Environ Energy 2024;350:123904.
[18] Seretis A, Tsiakaras P. Renew Energy 2016;85:1116–26.
[19] Chen G, Li W, Chen H, Yan B. J Zhejiang Univ - Sci 2015;16:491–506.
[20] Coronado I, Stekrova M, García Moreno L, Reinikainen M, Simell P, Karinen R, Lehtonen J. Biomass Bioenergy 2017;106:29–37.
[21] El Doukkali M, Iriondo A, Cambra JF, Gandarias I, Jalowiecki-Duhamel L, Dumeignil F, Arias PL. Appl Catal Gen 2014;472:80–91.
[22] Bossola F, Pereira-Hernández XI, Evangelisti C, Wang Y, Dal Santo V. J Catal 2017;349:75–83.
[23] Oliveira AS, Baeza JA, Calvo L, Alonso-Morales N, Heras F, Rodriguez JJ, Gilarranz MA. Appl Catal B Environ 2019;245:367–75.
[24] Kim H-D, Kim T-W, Park HJ, Jeong K-E, Chae H-J, Jeong S-Y, Lee C-H, Kim C-U. Int J Hydrogen Energy 2012;37:12187–97.
[25] Zoppi G, Pipitone G, Gruber H, Weber G, Reichhold A, Pirone R, Bensaid S. Catal Today 2021;367:239–47.
[26] Godina LI, Tokarev AV, Simakova IL, Mäki-Arvela P, Kortesmäki E, Gläsel J, Kronberg L, Etzold B, Murzin DYu. Catal Today 2018;301:78–89.
[27] Sousa J, Lakhtaria P, Ribeirinha P, Huhtinen W, Tallgren J, Mendes A. Catalysts 2024;14.
[28] Davda RR, Shabaker JW, Huber GW, Cortright RD, Dumesic JA. Appl Catal B Environ 2005;56:171–86.
[29] Li M, Ji W, Huang C, Si X, Liu Q, Lu R, Lu T. Catalysts 2025;15.
[30] Wen G, Xu Y, Xu Z, Tian Z. Catal Commun 2010;11:522–6.
[31] Soták T, Hronec M, Vávra I, Dobročka E. Int J Hydrogen Energy 2016;41:21936–44.
[32] Yu Y, Lou X, Wu H. Energy Fuels 2008;22:46–60.
[33] Kumar P, Barrett DM, Delwiche MJ, Stroeve P. Ind Eng Chem Res 2009;48:3713–29.
[34] Zhang J, Yan W, An Z, Song H, He J. ACS Sustainable Chem Eng 2018;6:7313–24.
[35] You SJ, Baek IG, Kim YT, Jeong K-E, Chae H-J, Kim T-W, Kim C-U, Jeong S-Y, Kim TJ, Chung Y-M, Oh S-H, Park ED. Kor J Chem Eng 2011;28:744–50.
[36] Zhang J, Zhu Y, An Z, Shu X, Ma X, Song H, Wang W, He J. ACS Appl Energy Mater 2020;3:7048–57.
[37] Wen G, Xu Y, Liu Q, Wang C, Liu H, Tian Z. Catal Lett 2011;141:1851–8.
[38] Directorate-General for Internal Market. Industry, entrepreneurship and SMEs (European Commission), Grohol, Milan, Veeh, constanze, Study on the critical raw materials for the EU 2023: final report. Publications Office of the European Union; 2023.
[39] Zhang J, Xu N. Catalysts 2020;10.
[40] Cesar DV, Santori GF, Pompeo F, Baldanza MA, Henriques CA, Lombardo E, Schmal M, Cornaglia L, Nichio NN. Int J Hydrogen Energy 2016;41:22000–8.
[41] Cavani F, Trifirò F, Vaccari A. Catal Today 1991;11:173–301.
[42] Altalhi AA, Mohamed EA, Negm NA. Energy Adv 2024;3:2136–51.
[43] You X, Chen L, He S, Zhang G. Catalysts 2023;14.
[44] Kanezaki E. Solid State Ionics 1998;106:279–84.
[45] Fasolini A, Lombardi E, Tabanelli T, Basile F. Nanomaterials 2021;11:1175.
[46] Hu X, Lievens C, Larcher A, Li C-Z. Bioresour Technol 2011;102:10104–13.
[47] dos Santos JB, de Albuquerque NJA, de CL, Zanta P e S, Meneghetti MR, Meneghetti SMP. RSC Adv 2015;5:90952–9.
[48] Wassenberg A, Esser T, Poller MJ, Albert J. Materials 2023;16.
[49] Shi N, Liu Q, Ju R, He X, Zhang Y, Tang S, Ma L. ACS Omega 2019;4:7330–43.
[50] Velasco Calderón JC, Arora JS, Mushrif SH. ACS Omega 2022;7:44786–95.
[51] Biesinger MC, Payne BP, Lau LWM, Gerson A, Smart RStC. Surf Interface Anal 2009;41:324–32.
[52] Zhang J, Zhu Y, An Z, Shu X, Ma X, Song H, Wang W, Zhao J, Cao X, He J. J Mater Chem A 2020;8:14697–705.
[53] Chen X, Wang X, Fang D. Fuller Nanotub Carbon Nanostructures 2020;28:1048–58.
[54] Di Cosimo JI, Díez VK, Xu M, Iglesia E, Apesteguía CR. J Catal 1998;178:499–510.
[55] Casenave S, Martinez H, Guimon C, Auroux A, Hulea V, Cordoneanu A, Dumitriu E. Thermochim Acta 2001;379:85–93.
[56] Gac W. Appl Surf Sci 2011;257:2875–80.
[57] Wang Z, Zhang T, Ramirez Reina T, Huang L, Xie W, Musyoka NM, Oboirien B, Wang Q. Fuel 2024;366:131383.
[58] Wierzbicki D, Baran R, Dębek R, Motak M, Grzybek T, Gálvez ME, Da Costa P. Int J Hydrogen Energy 2017;42:23548–55.
[59] Li Z, Wu P, Pang J, Li X, Zhai S, Zheng M. Catalysts 2023;13.
[60] Hata D, Aihara T, Miura H, Shishido T. J Jpn Petrol Inst 2021;64:280–92.
[61] Megías-Sayago C, Navarro-Jaén S, Drault F, Ivanova S. Catalysts 2021;11.
[62] Li X, Zhai Z, Tang C, Sun L, Zhang Y, Bai W. RSC Adv 2016;6:62252–62.
[63] van Dam HE, Kieboom APG, van Bekkum H. Starch - Stärke 1986;38:95–101.
[64] Karwa S, Gajiwala VM, Heltzel J, Patil SKR, Lund CRF. Catal Today 2016;263:16–21.
[65] Fasolini A, Martelli G, Piazzi A, Curcio M, De Maron J, Basile F, Mazzoni R. ChemCatChem 2024;16:e202400393.
[66] Pipitone G, Zoppi G, Frattini A, Bocchini S, Pirone R, Bensaid S. Catal Today 2020;345:267–79.
[67] de Vlieger DJM, Mojet BL, Lefferts L, Seshan K. J Catal 2012;292:239–45.
[68] Girisuta B, Janssen LPBM, Heeres HJ. Green Chem 2006;8:701–9.
[69] Matsumura Y, Yanachi S, Yoshida T. Ind Eng Chem Res 2006;45:1875–9.
[70] Deng T, Liu H. J Mol Catal Chem 2014;388–389:66–73.
[71] Davda RR, Dumesic JA. Chem Commun 2004:36–7.
[72] Gilea D, Lazar L, Carja G, Hussain CM, Bhattacharyya KG, Mallakpour S, Roy Chowdhury P, Medhi H, editors. Transit. Met.-Based layer. Double hydroxides chem. Appl. Cham: Springer Nature Switzerland; 2026. p. 409–25.